Highly ductile amorphous oxide at room temperature and high strain rate

20 authors, including:

Erkka J. Frankberg
Istituto Italiano di Tecnologia
11 PUBLICATIONS   36 CITATIONS

SEE PROFILE

Janne Kalikka
Tampere University
23 PUBLICATIONS   308 CITATIONS

SEE PROFILE

Turkka Salminen
Tampere University
46 PUBLICATIONS   172 CITATIONS

SEE PROFILE

Siddardha Koneti
Institut National des Sciences Appliquées de Lyon
24 PUBLICATIONS   31 CITATIONS

SEE PROFILE

Some of the authors of this publication are also working on these related projects:

Precipitation View project

pulsed laser deposition View project

Highly ductile amorphous oxide at room temperature and high strain rate

Authors: Erkka J. Frankberg[1,2,3,*], Janne Kalikka[4], Francisco García Ferré[3,†], Lucile Joly-Pottuz[2,*], Turkka Salminen[5], Jouko Hintikka[1], Mikko Hokka[1], Siddardha Koneti[2], Thierry Douillard[2], Bérangère Le Saint[2], Patrice Kreiml[6], Megan J. Cordill[6], Thierry Epicier[2], Douglas Stauffer[7], Matteo Vanazzi[3], Lucian Roiban[2], Jaakko Akola[4,8], Fabio Di Fonzo[3], Erkki Levänen[1] & Karine Masenelli-Varlot[2]

Affiliations:

[1] Tampere University, Materials Science and Environmental Engineering, Finland.

[2] Univ Lyon, INSA-Lyon, UCBL, MATEIS, CNRS UMR 5510, France.

[3] Istituto Italiano di Tecnologia, Center for Nano Science and Technology@PoliMi, Italy.

[4] Tampere University, Computational Physics Laboratory, Finland.

[5] Tampere University, Microscopy Center, Finland.

[6] Erich Schmid Institute of Materials Science, Austrian Academy of Sciences, Austria.

[7] Bruker Inc., USA.

[8] Norwegian University of Science and Technology, Department of Physics, Norway.

[†] Current affiliation: ABB Switzerland Ltd., Corporate Research, Switzerland.

[*] Corresponding authors: erkka.frankberg@tuni.fi, lucile.joly-pottuz@insa-lyon.fr .

Abstract: Oxide glasses are an integral part of the modern world, but their usefulness can be limited because of the characteristic brittleness at room temperature. We show that amorphous aluminum oxide (a-Al_2O_3) can permanently deform without fracture at room temperature and high strain rate by a viscous creep mechanism. These thin films can reach flow stress at room temperature and flow plastically up to 100 % total elongation, as long as the material is dense and free of geometrical flaws. Our observations show a much higher ductility at low temperature for an amorphous oxide than previous observations. The discovery may allow realization of damage tolerant glass materials that contribute in new ways, for example, to the mechanical resistance and reliability of future electronic devices and batteries.

One Sentence Summary: An oxide glass is revealed substantially more ductile at room temperature than what has been believed.

Main Text: Inorganic oxide glasses show great promise for modern electronics, including optoelectronics, flexible electronics, photovoltaics, single electron transistors and battery technologies (*1-6*). These glasses allow for a wide range of tailored, functional properties from full dielectrics to tuned semiconductors coupled with visible light transparency, and good chemical and thermal stability. However, in practical terms they are always considered brittle, which has led to the current design paradigm of glass and ceramic materials.

In the thermodynamics of inorganic glasses, relaxation mechanisms such as viscous flow and viscous creep are thought to require high temperatures to activate. Viscous flow and viscous creep are separated by a notion that creep is always activated by external loading in addition to thermal activation. Above a certain critical temperature, the glass transition temperature, T_g, bulk glass softens to a point where relaxation mechanisms activate and allow viscosity measurements. Viscosity is the proportionality factor of stress needed for a bulk glass to flow at a selected speed or strain rate. Below the glass transition temperature, creep of an inorganic glass under its own gravity is slowed down so much that it takes tens of millions of years to detect any permanent deformation by the viscous mechanisms (*7-10*). Therefore, in practice, we cannot make room temperature measurements of glass viscosity and an oxide glass below T_g is effectively considered a solid. The evidence for this is clear, but the current theory neglects the possibility of mechanical activation by an external stress field gradient, such as a gradient that occurs, for example, when a mobile device with a touch screen is dropped on a hard floor.

Moreover, oxide glasses are considered brittle at room temperature due to the lack of active plastic deformation mechanisms. Under critical elastic load, stress concentrates on the most

severe pre-existing geometrical flaw leading to a sudden, catastrophic failure (*11*). Nevertheless, the most profound evidence for plastic relaxation occurring in oxide glasses below the glass transition temperature is the simple hardness test. Hardness of a bulk glass or any other material is measured from the dimensions of a permanent residual indent made by a diamond indenter at room temperature. Permanent deformation is possible in glasses through diffusion-based mechanisms. Oxide glasses are known to permanently deform by densification (*12*) and shear flow (*13, 14*) under contact and hydrostatic loads. However, the plastic deformation mechanisms at room temperature are currently believed to be limited to geometrically confined loading modes, such as bulk indentation, and that brittleness always severely limits the use of glass structures under more realistic unconfined loading conditions such as bending and pulling. Experimental observations for Al_2O_3 at the nanoscale have been mixed: some measurements show prerequisites for plastic deformation at room temperature (*15-18*), while others display fully brittle behavior (*19-21*).

We provide evidence that under sufficient load the viscosity of amorphous Al_2O_3 thin films can be measured at room temperature. Furthermore, the viscous creep mechanism can induce large and fast permanent relaxation without substantial thermal activation. We consider the inorganic oxide glass to be in a super-cooled liquid state, even if far below the T_g. Under these conditions, the plastic relaxation requires a considerable external driving force, but we found that it is possible even within short time scales from seconds to nanoseconds.

We made micromechanical shear/compressive (Fig. 1A) and tensile (Fig. 1B) measurements along with atomistic simulations to determine the viscosity of defect-free amorphous Al_2O_3. The

viscosity of the a-Al$_2$O$_3$ follows a log-log linear power rule as a function of the strain rate (Fig. 1C). The power rule indicates that as the strain rate approaches zero, the viscosity of the super-cooled liquid approaches infinity, equivalent to a quasi-solid state as:

$$\lim_{\dot{\varepsilon} \to 0} \eta_{a-Al_2O_3}(\dot{\varepsilon}) = \infty \ . \hspace{3cm} \text{(eq. 1)}$$

We detected no transition from solid-like to liquid-like behavior, and, the viscosity must be a finite quantity for flow to occur in this super-cooled liquid state. There is a strong decrease in viscosity as the strain rate increases and notably low simulated viscosity values were measured at simulated strain rates over 10^8 1/s. Extrapolating the results to very high strain rates suggests a 1 Pa·s viscosity for a-Al$_2$O$_3$, comparable to glycerol at 300 K. This indicates that flow stress cannot substantially increase beyond the limit needed for atoms to diffuse through the glass network, which is reflected as a very low viscosity at very high strain rates.

We measured the viscosity during the plastic flow at flow stress, which is defined as the stress we measured after the glass structure yields. No contrast changes were detected in the samples either during the plastic flow or by ex situ observations using transmission electron microscopy (TEM). We believe these observations combined with no evidence for shear bands means the samples remained amorphous during the plastic deformation (22, Section S2). The simulated plastic flow stress in tensile (Fig. 2A) and compressive (Fig. 2B) loading agrees very well with their respective experimental results and, depending on the loading mode, a total strain of up to 100 % can be measured in situ along the loading axis without fracture. We were able to visually record (Fig. 2, insets) the dynamic plastic deformation throughout each experiment in addition to comparing to numerical data (22, Section S3).

We detected a fracture only in the experimental tensile test after 15 % of total strain and 5 - 8 % of plastic strain depending on the interpretation of the yield stress. We found that the fracture occurred in a localized region affected by ion damage, which is induced to the sample during sample preparation (22, Sections S4-S5). Ion damage leads to void nucleation, growth, and transformation into a sharp edge crack (Fig. S6), which eventually induced the fracture.

The scatter of flow stress values at varying strain rates is evidence of the time-dependent nature of the plastic flow we observed. A strain rate dependent flow stress is typically observed for viscoplastic materials (22), and would be an important piece of evidence of the viscous relaxation mechanisms active in a-Al_2O_3. The force variation we measured during flow stress is 2 - 3 orders of magnitude higher than the nominal noise floor of the force measurement of the experiment (Fig. 3A), which verifies the connection between stress and strain rate. When the strain rate is changed, the flow stress changes with the proportion given by the viscosity of the super cooled liquid and similar behavior is observed in both repeated experiments and simulations (Fig. 3).

The lack of contrast change in our TEM observations suggest that the cumulative plastic deformation was likely driven by homogenous diffusion. We used our material model to determine plausible atomistic mechanisms, which control the plastic deformation in a-Al_2O_3 at room temperature. The first activated plasticity mechanism from our model is related to the change in the glass density in both tensile and compressive loading. The simulated density has a permanent reduction under tensile load when returning to 1 atm pressure (Fig. 4A). The permanent decrease was by 0.5 – 1.4 %, which accounts for only 0.9 – 1.5 % of the permanent

elongation (or 0.006 – 0.021 in strain) of the model along the axis under tension. The density

saturates at 20 - 25 % of total tensile strain and at higher strains the plastic deformation takes

place solely by steady state viscous creep (Fig. 4A). We found flow stress saturation at ~ 25 % of

tensile strain (Fig. S5A) paralleling the density saturation.

5

Both plasticity phenomena occur by bond switching in our simulations, as showed by the

evolution of nearest-neighbor bonding in tension and in compression as a function of strain (Fig.

4B). The interchange and rotation of bonds, with the resulting atomic translocation, are fully

accommodated without density changes, which allow for more versatile deformation in shear and

10   tensile loading modes. This is supported by the unchanged coordination number as bond changes

during plastic flow are predominantly swaps, i.e. atoms retain the local environment while

changing neighboring atoms (Figs. 4B, S23 and S24).

The atomistic mechanisms of the plastic deformation we measured have local and collective

15   features (22, Section S6). Our simulations (D^2_{min}, $\Delta\varepsilon = 0.01$) show separate areas of high and

low plastic tensile strain that correlate with flow stress data (Fig. 4C - a). The diffusion of atoms

increases when the stress decreases, and vice versa (Figs. 4C – b and S10). Therefore, plasticity

in a-Al_2O_3 occurs when weaker local atomic groups are driven to yield by the accumulation of

individual bond switching events. An individual bond switching event is shown to occur at the

20   edge of a locally yielding atom group (Fig. 4C - c). In this event, the central Al (gold) initially

has 4 oxygen neighbors with open space next to it. The Al atom moves into the open space,

while replacing one oxygen bond with a new one. After this, it moves farther and gains two new

oxygen neighbors that are kept for approximately 150 ps. The Al atom stays bonded to 5 oxygen

atoms until the end of loading. This type of bond switching is well known to occur in disordered materials (*23, 24*). Over a large cumulative strain, the localized plastic strain events vary randomly (Movie S1) to accumulate an overall homogenous plastic flow across the structure. The distribution of the cumulative plastic tensile strain (D^2_{min}, $\Delta\varepsilon = 0.5$) has intertwined areas of

5 high and low D^2_{min} with no large volumes of either (Fig. 4D, for compression, see Fig. S11). This shows that the cumulative atomic movement related to plastic flow is homogeneous across the structure, with momentary large fluctuations. The fast relaxation we observed by atomic diffusion occurs far below the bulk $T_g \approx 973$ K (*25*), which is not anticipated by the thermodynamic theory of inorganic glasses.

10

We considered several potential issues that could result in spurious results. Sample heating from the electron beam is limited to a maximum of 5 K (*26*) and plastic strain induced adiabatic heating only occurs after yielding (22, Sections S7-S8). Adiabatic heating may contribute to our observed flow stress magnitude. Electron beam damage can decrease flow stress, as has been

15 observed for amorphous SiO_2 (a-SiO_2) (*23, 27*). We performed a dedicated mechanical test, in which the electron beam is switched OFF during the steady state viscous creep of the a-Al_2O_3 thin film (22, Section S9). The flow stress level does not change enough when the beam is OFF for us to interpret it to occur outside the normal stress fluctuation caused by the dynamic strain rate. We performed multiple experiments in full beam-OFF conditions that verified this behavior.

20 Together these experiments rule out the possibility that the electron beam had a substantial effect on the experimental test results. Moreover, it is possible to induce plasticity in amorphous oxides via a "size effect" by dramatically increasing the ratio of surface atoms to bulk atoms (*18, 24*). However, our sample dimensions lead to bulk-like properties such as T_g and fracture toughness

(22, Section S10). The measured $K_{Ic} = 3.1 \, MPa\sqrt{m}$ is similar to typical bulk Al_2O_3 but since our initial flaw size was measured in situ to be sufficiently small or non-existent, the stress field can reach a magnitude in which the material yields, even at room temperature. We also modified the molecular dynamic simulation setup for a-Al_2O_3, i.e. cell size and quenching method, to rule out artificial ductility and observed no fracture (22, Sections S11-S12).

Our results for a-Al_2O_3 differ from the previous results obtained for a-SiO_2 (*23, 24, 27*). Bulk tensile plastic flow has not been observed in free standing membranes or nanowires of a-SiO_2 at ambient conditions (*24, 27*). Densification accounts for 80 - 90 % of the measured plastic deformation during indentation for a-SiO_2 (initiated between 9 - 13 GPa stress, at RT) that activates before viscous creep (*13, 28*). Tensile experiments with pristine a-SiO_2 samples under ambient conditions have reached only up to approximately 5 GPa before fracture (*24, 27*), therefore, finding zero plasticity at this stress level is not surprising. A tensile fracture is likely initiated by the intrinsic and interconnecting cavities (voids, free volume) found in the atomic structure of a-SiO_2 (*29*), which are far more abundant in a-SiO_2 (65.7 Vol. %, (*30*)), than in a-Al_2O_3 (8.7 Vol. %) (22, section S13). The difference in cavity volumes is in line with the difference in atom densities as a-SiO_2 has 0.066 atoms/$Å^3$ (*31*) while a-Al_2O_3 has approximately one third higher atom density. The intrinsic cavities present in the a-SiO_2 structure were proposed to be the possible origin of fracture already in 2003 by Célarié *et al.* (*32*) and, since then, mechanical properties of a-SiO_2 and the presence of cavities has been studied further with experiments and simulations (*24, 27, 29, 30*).

8

Bond switching is also one source for mechanical relaxation in a-SiO$_2$ (*23, 24*). However, simulations show an 8 - 25 times greater potential for bond switching in a-Al$_2$O$_3$ compared to a-SiO$_2$ (*24*) explaining the large plastic strain we observed in a-Al$_2$O$_3$ (22, section S11). Under tension, the pre-existing cavities spatially inhibit bond switching from occurring in the a-SiO$_2$ structure, which likely results in further cavitation and fracture at low or zero plastic strain. Therefore, the pre-existing cavities in the atomic structure of a-SiO$_2$ coupled with the relatively high yield stress of a-SiO$_2$ present the most plausible hypothesis for the cause of tensile brittleness in amorphous SiO$_2$.

We conclude that in parallel to flawlessness, the other main boundary condition for a-Al$_2$O$_3$ ductility at room temperature is the intrinsically low effective activation energy, which is estimated to be $Q_{a-Al_2O_3} = 117.3 \pm 4.5$ kJ/mol (22, section S14), in good accordance with previous observations (*33*). This leads to plastic relaxation of a-Al$_2$O$_3$ by a stress gradient, because the stress concentrated on any pre-existing flaw (of intrinsic or manufacturing origin) remains below the critical value needed for fracture. Therefore, the flaw distribution coupled with the effective activation energy establish a criterion under which other inorganic oxide glasses may or may not achieve similar plasticity. This criterion provides a plausible path to find other oxide materials with similar ductile behavior and to explain the origin of such behavior. In addition, a high Poisson's ratio measured for a-Al$_2$O$_3$ (*16*) could indicate potential plasticity also in other oxides. Theoretically, there are no restrictions to apply the criterion to macroscopic bulk glasses. Instead, the challenge appears fully technological since we lack processing technology that could produce such flaw free amorphous materials at a macroscopic scale. Specifically to Al$_2$O$_3$, the challenge is also related to the low glass forming capability. Conventional melt

quench techniques typically fail to prevent crystallization of pure Al_2O_3 and it essentially requires an extreme quenching rate (e.g. Pulsed laser deposition) or low temperature (e.g. Atomic layer deposition) processing route to retain the amorphous structure. Nevertheless, our results give much needed insight on the viscous relaxation behavior of inorganic glasses below the T_g and present tools to further study the thermodynamic theory of super-cooled liquids. To improve the theory, we propose that in addition to thermal activation, mechanical activation is equally and independently capable of inducing relaxation of a glass network.

In summary, we have shown that amorphous aluminum oxide is a substantially more ductile material than what has been believed. The results indicate that plasticity by the viscous creep mechanism requires a dense and flaw-free glass network coupled with an effective activation energy that allows sufficient bond switching activity. In addition to oxide thin films already applicable in electronics and batteries, for example, amorphous oxides show potential to be used as high strength, damage tolerant engineering materials. In order to realize the potential, we face a challenge to develop manufacturing and characterization technologies that allow controlling the material flaws in the atomic structure and at the nanoscopic scale.

References and Notes:

1.   X. Yu *et al.,* Metal oxides for optoelectronic applications. *Nat. Mater.* **15**, 383–396 (2016)

2.   K. Nomura *et al.,* Room-temperature fabrication of transparent flexible thin-film transistors using amorphous oxide semiconductors. *Nature* **432**, 488-492 (2004)

3.   H. Hosono *et al.,* Transparent amorphous oxide semiconductors for organic electronics: Application to inverted OLEDs. *PNAS* **114:2**, 233-238 (2017)

4. G. Karbasian *et al.,* Metal-Insulator-Metal Single Electron Transistors with Tunnel Barriers Prepared by Atomic Layer Deposition. *Appl. Sci.* **7:3**, 246 (2017)

5. J. Y. Kim *et al.,* New Architecture for High-Efficiency Polymer Photovoltaic Cells Using Solution-Based Titanium Oxide as an Optical Spacer. *Adv. Mater.* **18**, 572–576 (2006)

6. Y. Idota *et al.,* Tin-Based Amorphous Oxide: A High-Capacity Lithium-Ion-Storage Material, *Science* **276:5317**, 1395-1397 (1997)

7. E. D. Zanotto, Do cathedral glasses flow? *Am. J. Phys.* **66**, 392 (1998)

8. E. D. Zanotto *et al.,* Do cathedral glasses flow?—Additional remarks. *Am. J. Phys.* **67**, 260 (1999)

9. J. Zhao *et al.,* Using 20-million-year-old amber to test the super-Arrhenius behaviour of glass-forming systems. *Nat. Commun.* **4**, Article number: 1783 (2013)

10. Y. Yu *et al.,* Stretched Exponential Relaxation of Glasses at Low Temperature. *Phys. Rev. Lett.* **115**, 165901 (2015)

11. A. A. Griffith, The Phenomena of Rupture and Flow in Solids. *Phil. Trans. R. Soc.* **A221**, 163-198 (1921)

12. F. M. Ernsberger, Role of densification in deformation of glasses under point loading. *J. Am. Ceram. Soc.* **51:10**, 545–547 (1968)

13. T. Rouxel *et al.,* Indentation deformation mechanism in glass: Densification versus shear flow. *J. Appl. Phys.* **107**, 094903 (2010)

14. G. Kermouche *et al.* Perfectly plastic flow in silica glass. *Acta Mater.* **114**, 146 – 153 (2016)

15. E. Calvié *et al.,* Real time TEM observation of alumina ceramic nano-particles during compression. *J. Eur. Ceram. Soc.* **32:10**, 2067-2071 (2012)

16. F. García Ferré *et al.,* The mechanical properties of a nanocrystalline Al2O3/a-Al2O3 composite coating measured by nanoindentation and Brillouin spectroscopy. *Acta Mater.* **61:7**, 2662-2670 (2013)

17. A. S. Esmaeily *et al.,* Exceptional room-temperature plasticity in amorphous alumina nanotubes fabricated by magnetic hard anodisation. *Nanoscale* **9**, 5205-5211 (2017)

18. Y. Yang *et al.* Liquid-like, self-healing aluminum oxide during deformation at room temperature. *Nano Lett.* **18**, 2492 − 2497 (2018)

19. A. van der Rest *et al.,* Mechanical behavior of ultrathin sputter deposited porous amorphous Al$_2$O$_3$ films. *Acta Mater.* **125**, 27-37 (2017)

20. D. Mercier *et al.,* Investigation of the fracture of very thin amorphous alumina film during spherical nanoindentation. *Thin Solid Films* **638**, 34-47 (2017)

21. S-H. Jen *et al.,* Critical tensile and compressive strains for cracking of Al$_2$O$_3$ films grown by atomic layer deposition. *J. Appl. Phys.* **109**, 084305 (2011)

22. A. Malkin *et al.,* A modern look on yield stress fluids. *Rheol. Acta* **56:3**, 177–188 (2017)

23. K. Zheng *et al.,* Electron-beam-assisted superplastic shaping of nanoscale amorphous silica. *Nat. Commun.* **1**, Article number: 24, (2010)

24. J. Luo *et al.,* Size-dependent brittle-to-ductile transition in silica glass nanofibers. *Nano Lett.* **16:1**, 105–113 (2016)

25. S. K. Lee *et al.,* Probing of 2 dimensional confinement-induced structural transitions in amorphous oxide thin film. *Sci. Rep.* **4**, Article number: 4200 (2014)

26. R. Nakamura *et al.,* Atomic rearrangements in amorphous Al2O3 under electron-beam irradiation. *J. Appl. Phys.* **113**, 064312 (2013)

27. M. Mačkovic *et al.,* A novel approach for preparation and in situ tensile tensting of silica glass membranes in the transmission electron microscope. *Frontiers in materials* 4:10, (2017)

28. D. Wakabayashi *et al.,* Compression behavior of densified SiO2 glass. *Phys. Rev. B* **84**, 144103 (2011)

29. S. Kohara *et al.,* Relationship between topological order and glass forming ability in densely packed enstatite and forsterie composition glasses. *PNAS* **108:36**, 14780-14785 (2011)

30. M. Murakami *et al.* Ultrahigh-pressure form of SiO_2 glass with dense pyrite-type crystalline homology. *Phys. Rev. B* **99**, 045153 (2019)

31. S. Kohara *et al.,* Lead silicate glasses: Binary network-former glasses with large amounts of free volume. *Phys. Rev. B* **82**, 134209 (2010)

32. F. Célarié *et al.* Glass Breaks like Metal, but at the Nanometer Scale. *Phys. Rev. Lett.* **90**, 075504 (2003)

33. R. Nakamura *et al.* Diffusion of oxygen in amorphous Al_2O_3, Ta_2O_5, and Nb_2O_5. *J. Appl. Phys.* **116**, 033504 (2014)

34. M. Matsui, Transferable Interatomic Potential Model for Crystals and Melts in the System CaO-MgO-Al2O3-SiO2. *Phys. Chem. Miner.* **23**, 571-572 (1996)

35. M. Matsui, Molecular dynamics study of the structures and bulk moduli of crystals in the systems CaO-MgO-Al2O3-SiO2. *Phys. Chem. Miner.* **23**, 345-353 (1996)

36. M. Matsui, M. Molecular dynamics simulation of structures, bulk moduli, and volume thermal expansivities of silicate liquids in the system CaO-MgO-Al2O3-SiO2. *Geophys. Res. Lett.* **23**, 395-398 (1996)

37. A. B. Belonoshko, Melting of corundum using conventional and two-phase molecular dynamic simulation method. *Phys. Chem. Miner.* **25**, 138-141 (1998)

38. R. Ahuja *et al.,* Melting and liquid structure of aluminum oxide using a molecular-dynamics simulation. *Phys. Rev. E.* **57**, 1673-1676 (1998)

39. G. Gutiérrez *et al.,* Structural properties of liquid Al_2O_3: A molecular dynamics study. *Phys. Rev. E.* **61**, 2723-2729 (2000)

40. G. Gutiérrez *et al.*, Molecular dynamics study of structural properties of amorphous Al2O3. *Phys. Rev. B.* **65**, 104202 (2002)

41. S. Plimpton, Fast Parallel Algorithms for Short-Range Molecular Dynamics. *J. Comp. Phys.* **117**, 1-19 (1995)

42. I. Heimbach *et al.,* pyMolDyn: Identification, structure, and properties of cavities/vacancies in condensed matter. *J. Comput. Chem.* **38**, 389–394 (2016)

43. M. L. Falk *et al.* Dynamics of viscoplastic deformation in amorphous solids. *Phys. Rev. E* **57**, 7192 (1998)

44. H. A. Barnes, A handbook on elementary rheology. University of Wales 200 p. (2000)

45. A. P. Minor *et al.,* Quantitative in situ nanoindentation in an electron microscope, *Appl. Phys. Lett.* **79:11** 1625-1627 (2001)

46. Z. Polo *et al.,* On the Taylor-Quinney coefficient in dynamically phase transforming materials: Application to 304 stainless steel. *Int. J. Plast.* **40**, 185 – 201 (2013)

47. D. A. Ditmars *et al.*, Enthaply and heat-capacity standard reference material: synthetic sapphire (α-Al2O3) from 10 to 2250 K. *J. Res. Natl. Bur. Stand.* **87:2**, 159 (1982)

Supplementary Materials:

Materials and Methods

Supplementary Text

Figs. S1-S24

5   Tables S1-S3

References (*34-47*)

Movie S1

A
Shear/compression
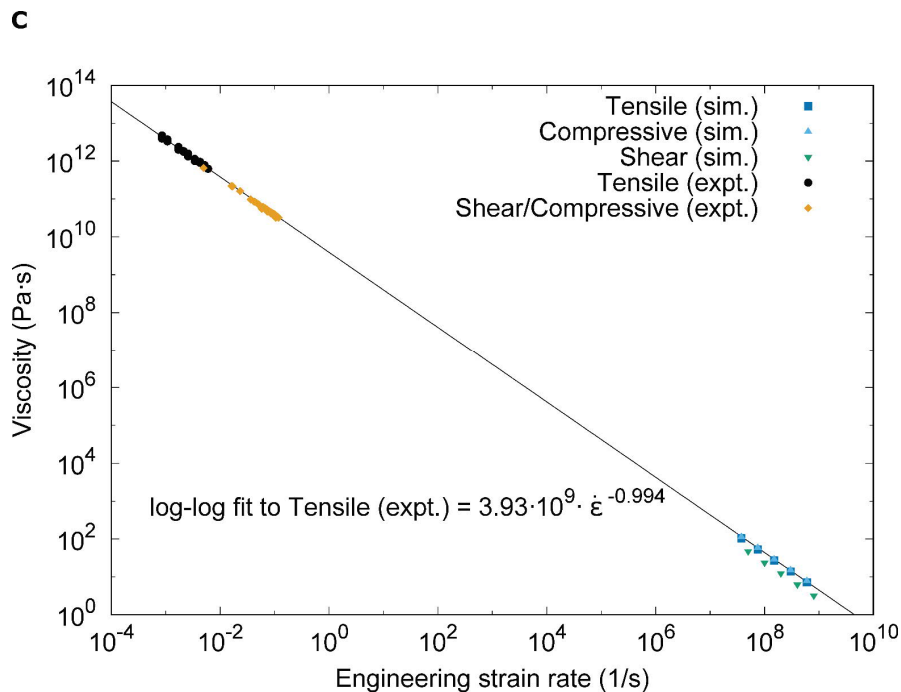

B
Tensile

C
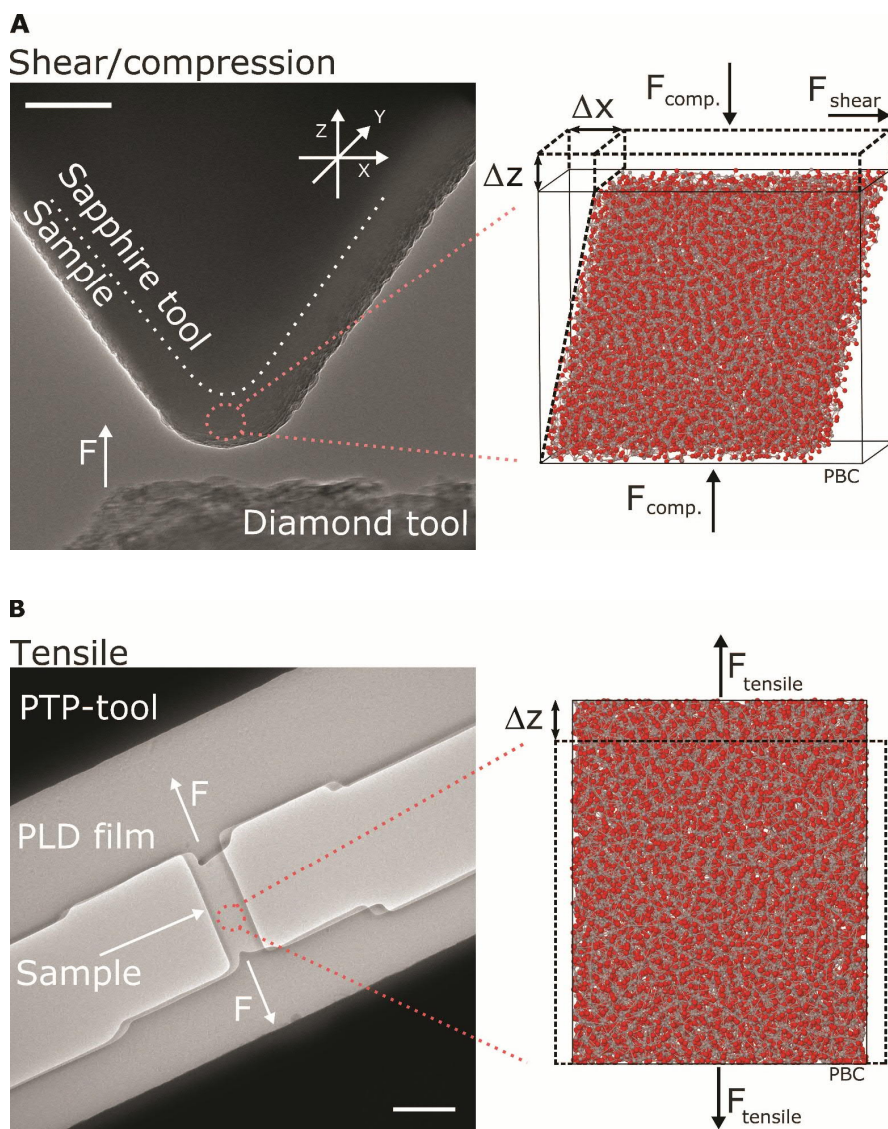
Fig. 1. Experimental and simulation procedures to measure the viscous behavior of amorphous Al₂O₃ at ≈ 300 K. (**A**) In situ experimental (expt.) shear/compressive setup (22, Section S1) and simulation (sim.) setups for separate shear and compression to measure the permanent deformation (strain) and flow of amorphous Al₂O₃ (sample). Scale bar 100 nm. (**B**) In situ experimental (push-to-pull, PTP) and simulation setups to measure permanent deformation and flow of amorphous Al₂O₃ (sample) under tension. Scale bar 1 μm. (**C**) Experimental and simulated viscosities (Log₁₀) as a function of strain rate (Log₁₀) during plastic flow. Simulated flow stress averaged between 25 – 50 % total strain (N = 6 for each data point). All simulations were performed with periodic boundary conditions (PBC) to simulate bulk behavior.
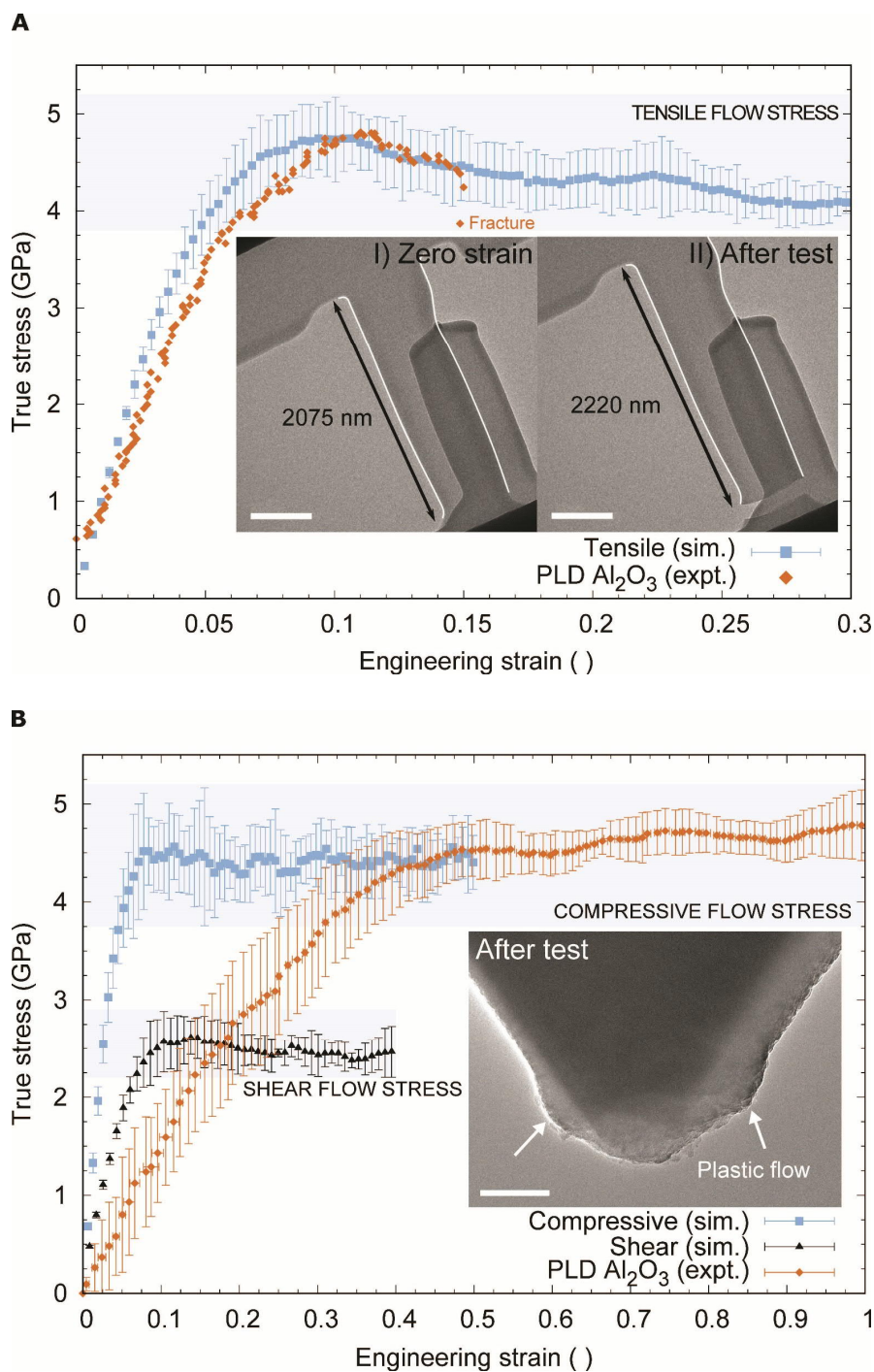
Fig. 2. Mechanical response of amorphous Al$_2$O$_3$ at room temperature: simulations and experimental data. (**A**) Average simulated (N = 30) and experimental (Beam ON, N = 1) tensile stress as a function of strain, inset I) shows the length of the free-standing tensile sample at the

onset of elastic contact (strain 0.0) and inset II) shows the length of the tensile sample after its fracture from the bottom part (scale bar 500 nm). In the insets, the sample is highlighted with white borders, while another piece of the pulsed laser deposited film partially overlaps the sample in the image but does not interact with the sample during the test. (**B**) Average simulated (N = 30) and average experimental (Beam OFF, N = 7) shear/compression stress as a function of strain, while the inset shows a deformed sample after the test (scale bar 100 nm). Note that the experimental true stress is a compound of mixed shear and compression loading. Simulated error bars show the maximum variation (min/max) measured with different strain rates ($37.5 \times 10^6 - 6.0 \times 10^8$ 1/s), while experimental error bars show standard deviation between samples.

A
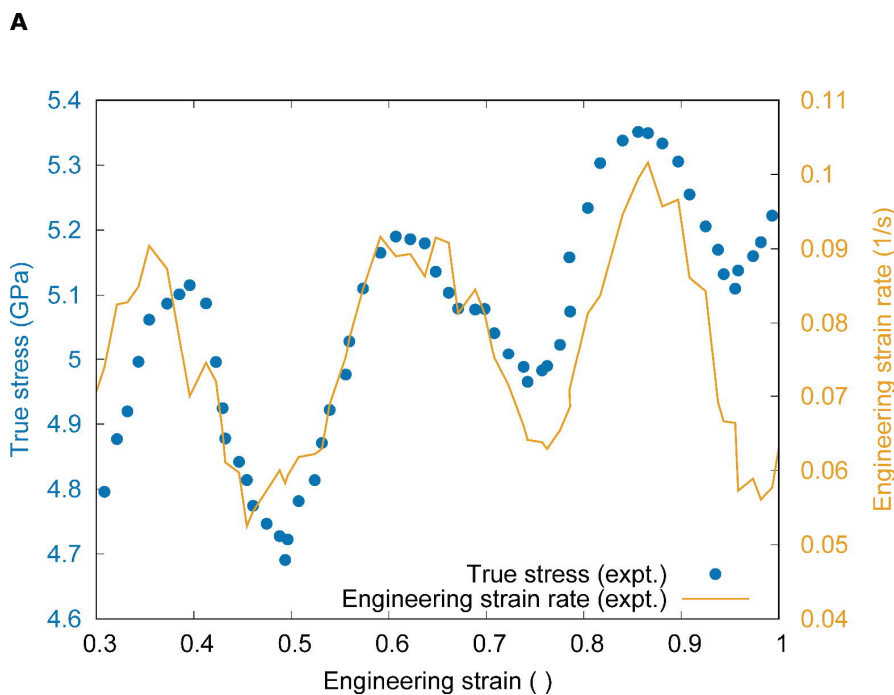
B
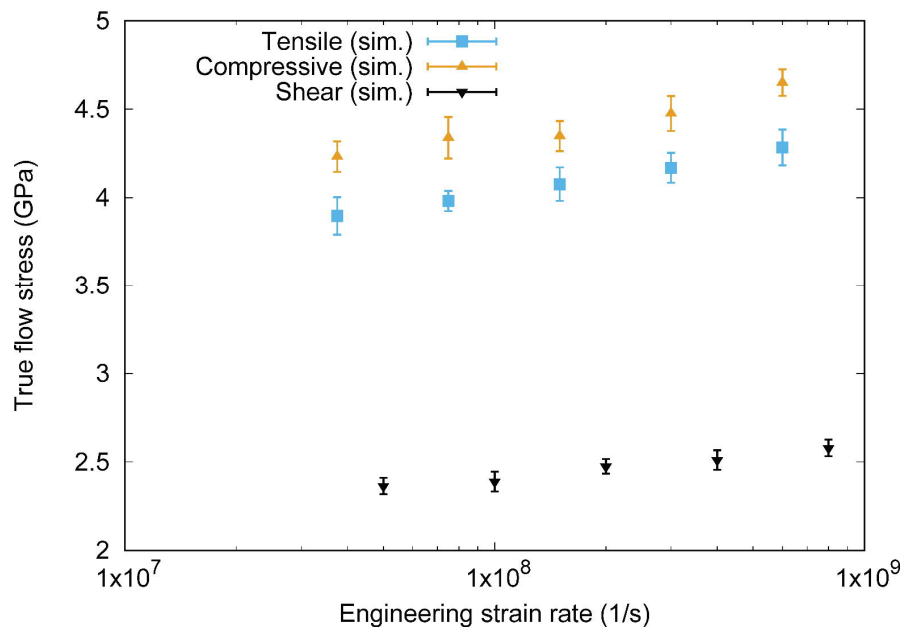
Fig. 3. Time dependent flow behavior of a-Al$_2$O$_3$ at room temperature: experimental and simulations. (A) Experimental flow stress and strain rate as a function of strain from a dedicated in situ TEM shear/compression test (electron beam ON, N = 1). The strain rate is measured using image correlation and the data is filtered using the Savitzky-Golay method with 22 points of window and a 5th order polynomial with the Origin software. Strain rate varies dynamically during the experimental measurement. True stress (GPa) on the left scale and engineering strain rate (1/s) on the right scale. **(B)** Averaged simulated (N = 6 for each data point) flow stress as a function of the strain rate measured and averaged between total strain of 25 - 50 %, error bars show standard deviation.

A

B

C

D

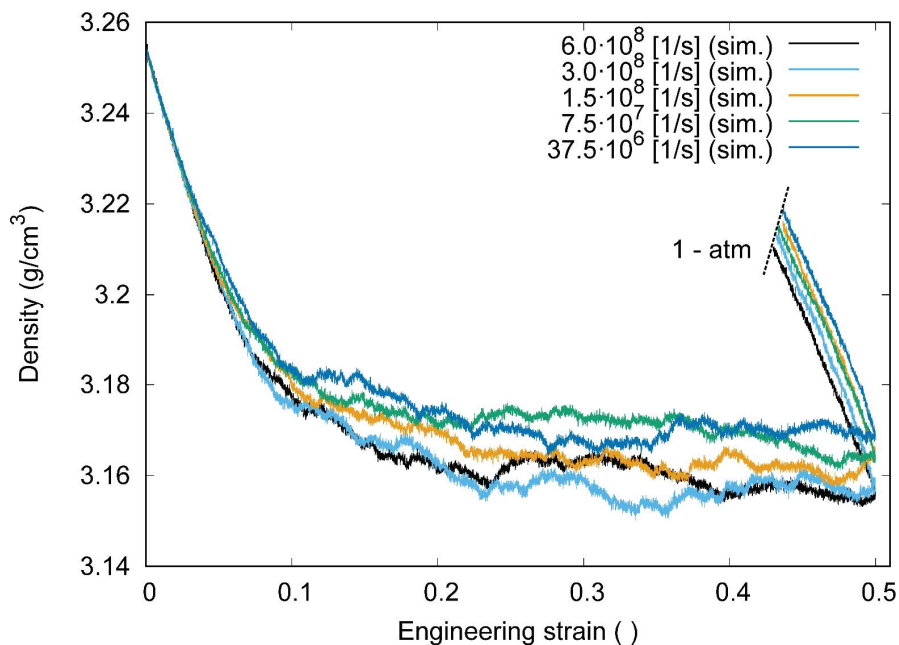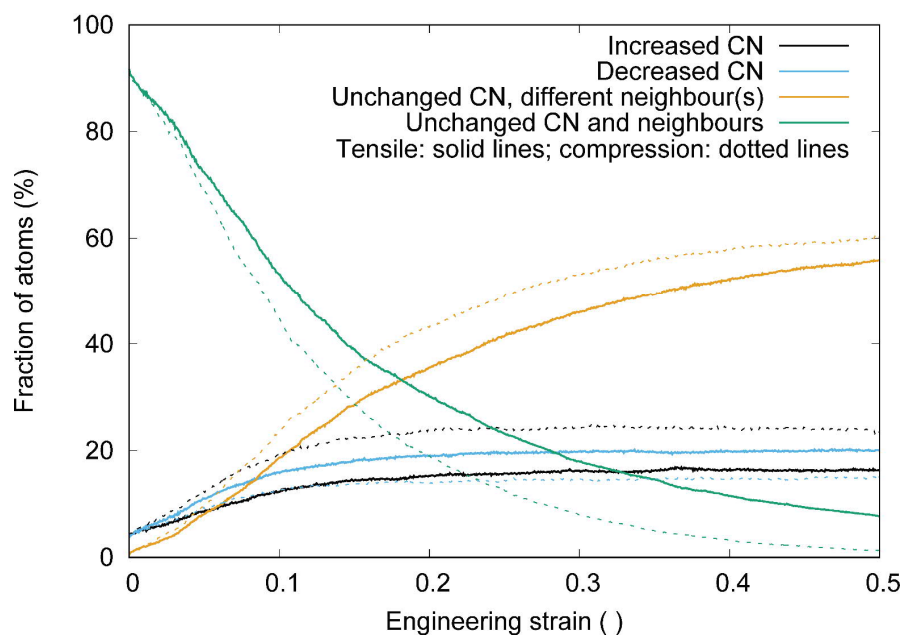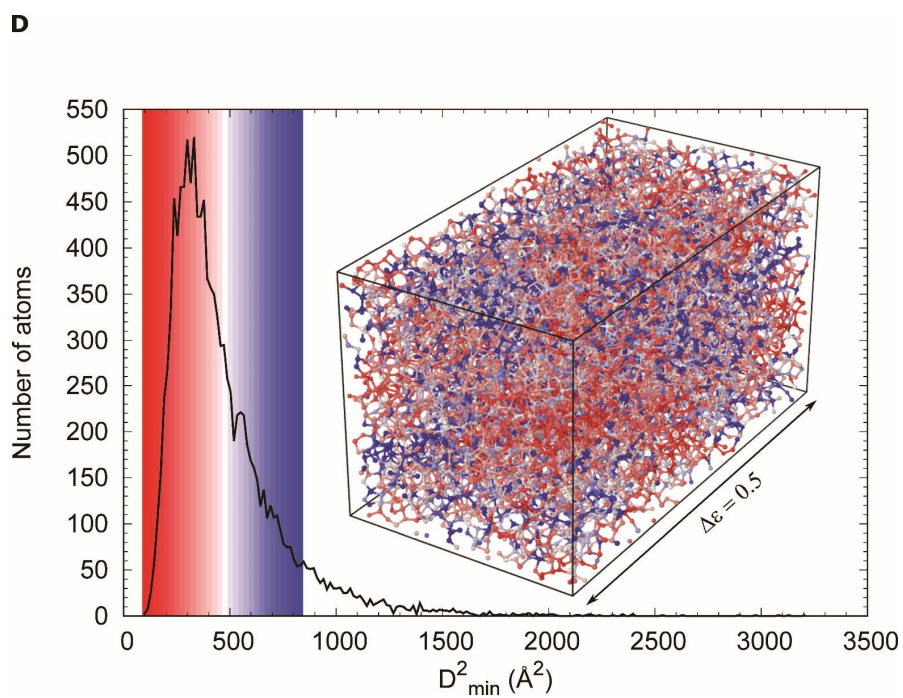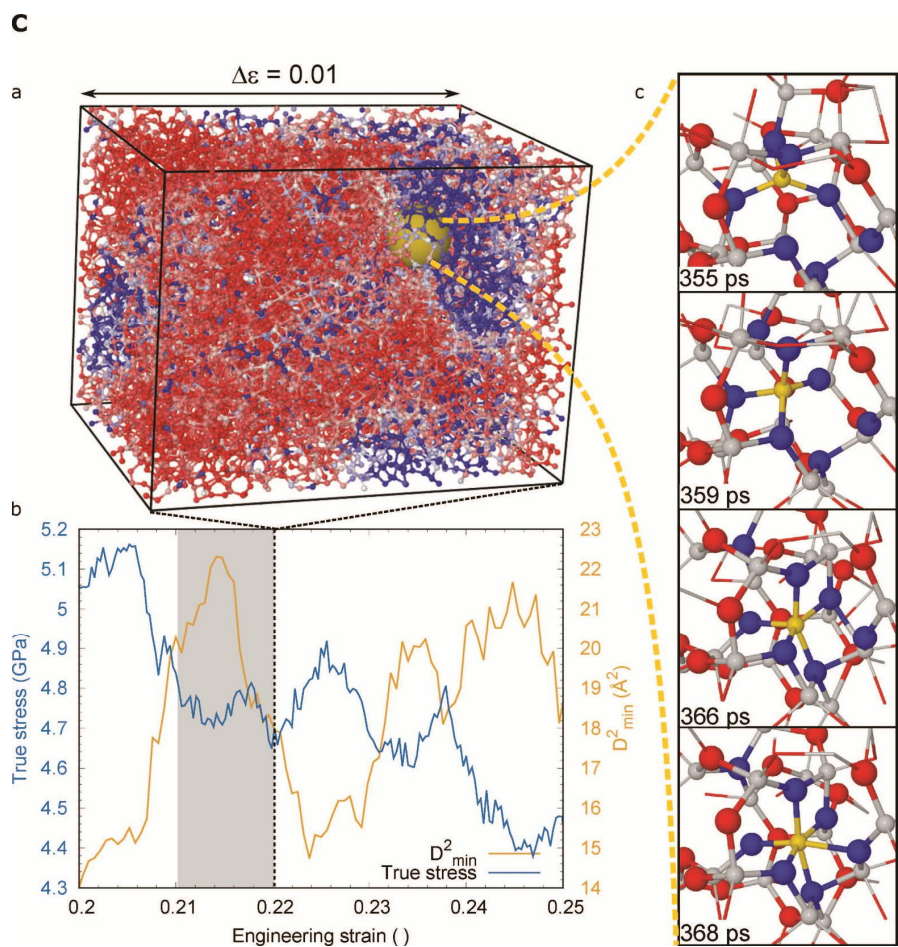**Fig. 4. Plasticity mechanisms in amorphous Al_2O_3.** (**A**) Average simulated density (N = 6) of a-Al_2O_3 during tensile loading, starting from and ending at atmospheric pressure (1 atm). (**B**) Average changes (N = 3) in bonding during tensile and compressive loading from 0.0 to 0.5 strain at 37.5 x 10^6 1/s strain rate (CN = coordination number). (**C**) Atomistic mechanism of room temperature plastic deformation in a-Al_2O_3; (a) momentary distribution of the local plastic tensile strain at 0.22 strain, where D^2_{min} is calculated from the preceding $\Delta\varepsilon$ = 0.01 indicated by grey color in (b), which in addition shows the correlation between D^2_{min} and flow stress data (N = 1); (c) a single bond switching event occurring at the edge of a locally yielding atom group (Colors: central Al: gold, oxygen bound at least once to the central Al: blue, Al: grey, O: red). Strain rate of 6.0 x 10^8 1/s corresponds to $\Delta\varepsilon$ = 0.01 in 16.67 ps. (**D**) Cumulative distribution of plastic tensile strain (D^2_{min}, $\Delta\varepsilon$ = 0.5) in the a-Al_2O_3 simulation cell between initial and final structure (7.5 x 10^7 1/s). Using a sliding color scale, atoms with below average D^2_{min} are colored shades of red, average D^2_{min} white, and above average D^2_{min} shades of blue. All atoms above the color scale are also colored blue. Loading axes shown by arrows.

Science

AAAS

Supplementary Materials for

Highly ductile amorphous oxide at room temperature and high strain rate

Authors: Erkka J. Frankberg[1,2,3,*], Janne Kalikka[4], Francisco García Ferré[3,†], Lucile Joly-Pottuz[2,*], Turkka Salminen[5], Jouko Hintikka[1], Mikko Hokka[1], Siddardha Koneti[2], Thierry Douillard[2], Bérangère Le Saint[2], Patrice Kreiml[6], Megan J. Cordill[6], Thierry Epicier[2], Douglas Stauffer[7], Matteo Vanazzi[3], Lucian Roiban[2], Jaakko Akola[4,8], Fabio Di Fonzo[3], Erkki Levänen[1] & Karine Masenelli-Varlot[2]

Correspondence to: erkka.frankberg@tuni.fi, lucile.joly-pottuz@insa-lyon.fr

This PDF file includes:

Materials and Methods
Supplementary Text
Figs. S1 to S24
Tables S1 to S3
Caption for Movie S1

Other Supplementary Materials for this manuscript includes the following:

Movie S1

Materials and Methods

Atomistic simulations

We adopted the classical force field of Matsui (*34*), which has been thoroughly tested for various phases of Al_2O_3 (*35-40*) and shown to accurately reproduce material properties such as density, bulk modulus and melting temperature. This is a model that would work well across the different phases and local structures encountered during straining simulations. All simulations were performed using LAMMPS simulation software (*41*) with 1 fs time step and periodic boundary conditions (PBC). A Nosé-Hoover thermostat and barostat, as implemented in LAMMPS, were used for temperature and/or pressure control. Cell deformations were achieved by changing the cell dimensions in very small increments every 100 fs to avoid artefacts produced by abrupt changes. The changes in the direction of strain were predefined, and the changes in the perpendicular directions were controlled by barostat, keeping the pressure at ambient value in those directions.

The amorphous base structure was generated similarly to the process described by Gutiérrez et al. (*40*). Initially a random structure of alumina with the density of 2.75 g/cm3 is equilibrated at 5000 K for 45 ps in NVT conditions to erase any structural memory, the structure is then cooled down to 3000 K over 10 ps, and equilibrated at that temperature for 45 ps. The density is then changed to 3.175 g/cm3, and the structure is equilibrated for further 45 ps before cooling it down to 650 K over ~650 ps at the rate of ~3.61 K/ps, and equilibrating it for 35 ps at that temperature. The pressure at this stage is -1.8 GPa.

Smaller cubic pieces of this structure were then used for straining simulations. The initial structures used in the simulations described in this article were cubes of 50 Å in each direction. The cut-outs were equilibrated at 300 K for hundreds of picoseconds (typically 500 - 700 ps, of which last 300 ps with NPT at zero pressure) to ensure that the artefacts related to cutting the simulation cell smaller were relaxed and that the structure was close to zero pressure in all three directions. The straining simulations were performed at a nominal temperature of 300 K with a thermostat. See Supplementary Text section S15 for detailed characterization of the simulated structures.

The cavities were calculated using surface-based cavity algorithm in pyMolDyn program (*42*) version 0.9.7, with ~ 0.1 Å grid spacing for the cavity domain search. The grid spacing was checked for convergence by recalculation with slightly different spacing values. The cut-off radius used to calculate cavities in a-Al_2O_3 (2.3 Å) was 9.5 % longer than the cut-off used for a-SiO_2 (2.1 Å) by Murakami et al. (*30*), which both correspond to the first minimum of the g(r) of the corresponding material.

In the simulations, the atoms were considered bonded if they were within 2.25 Å from each other. The cut-off is based on the partial pair correlation functions and it is within the first minimum of Al-O g(r) and before the first peak of Al-Al or O-O g(r). The bonding network was then used in coordination number, bond switching and bond angle analysis. Coordination number is simply the number of atoms within 2.25 Å. Bond switching analysis compares the coordination number and the neighboring atom ID numbers to the initial structure. If the coordination is changed, then the atoms are labelled as having increased or decreased coordination. If the coordination number is unchanged but the set of neighboring atoms has changed from the initial structure, then the atom is counted as unchanged CN with different neighbor(s).

We chose the D^2_{min} descriptor by Falk & Langer to indicate the local non-affine displacement of atoms during plastic deformation. For detailed mathematical formulation, see (*43*). Here, a linear strain field is fitted to the atomic displacements so that the mean-square difference between atomic displacements due to the strain field and the actual displacements is as small as possible. The D^2_{min} is then the mean-square of the residual displacement, i.e. displacement not due to the fitted strain field.

Thin film deposition

All samples were processed at room temperature using nanosecond UV laser (248 nm) by Pulsed Laser Deposition (PLD) to grow thin Al_2O_3 layers on substrates that included cleaved sodium chloride (NaCl) single crystals and shear/compression sapphire tools (R-plane sapphire single crystal rectangles 2 x 2 mm x 75 μm). The samples were coated using a pulse repetition rate of 20 Hz, a laser fluence of 3.5 J/cm^2 with a pulse energy of 400 mJ, and a background O_2 gas pressure of 0.1 Pa. Deposition was done in two batches, one for the shear/compression samples and one for the tension samples. The target-to-substrate distance was fixed at 50 mm. The substrate holder allowed the growth of the coatings on several substrates at a time by rotating the holder at a speed of 10 rpm. The target used for PLD was made of 99.99 % pure polycrystalline alpha aluminum oxide to produce films with a nominal thickness of 40 nm in the case of tensile test specimens and 60 nm in the case of shear/compressive test specimens.

TEM characterization

Obtained a-Al_2O_3 thin films were characterized in transmission electron microscopes (JEOL 2010F TEM 200 kV, FEI Titan ETEM 300 kV) to study the elemental composition with energy dispersive X-ray spectroscopy and scanning transmission electron microscopy, phase composition (amorphous/crystalline) with electron diffraction and nanostructures using high-resolution imaging. Electron tomography was performed on the in situ shear/compression tools to characterize their dimensions (see Supplementary Text section S1). The a-Al_2O_3 thin films reactivity against the high-energy electron beam was carefully studied to avoid any changes in the glass structure during mechanical experiments.

In situ TEM mechanical testing

Experimental mechanical testing was performed in the transmission electron microscope (FEI Titan ETEM, 300 kV) by using a nanomechanical-testing device fitted inside the TEM sample holder (PicoIndenter PI95, Hysitron/Bruker Inc.). The device has a nominal load noise floor of 200 nN with 1 mN maximum force and a nominal displacement resolution of ≤ 0.02 nm. Experiments consist of two loading modes: mixed shear/compression mode and tensile mode. To further study the electron beam effect, three imaging modes were used: first, the TEM electron beam was ON during the tests, secondly, the electron beam was switched OFF during the tests or thirdly, the electron beam was initially ON during the test and switched OFF during plastic deformation.

The dedicated shear/compression test setup consists of an electron transparent single crystalline sapphire tool, which is directly coated with a thin film sample without the need for further preparation (see Supplementary Text section S1). The tool and the sample are placed on a rigid mount and then fixed onto the nanomechanical-testing device. The sapphire tool has an apex angle of ~ 70° to allow unconfined deformation and to induce shear loading on the sample. To conduct an experiment, a diamond tool of the nanomechanical-testing device is aligned with

the sample and moved against the thin film sample. In total 14 samples were tested using this setup. During the deformation process, force and displacement are recorded in situ by the nanomechanical-testing device and the displacements are verified by TEM image correlation when beam ON conditions apply.

5   The dedicated tensile test setup consists of a commercial "push-to-pull" (PTP) device (Hysitron/Bruker Inc.) and a thin film sample transported onto the PTP device using a floating technique. In the floating technique, first the PLD film is coated on a freshly cleaved single crystal NaCl ([100] crystal orientation). Then the film is detached by submerging the NaCl cube in water leaving the thin film floating on water surface. The film is then collected on the PTP

10   device. The large-area films are finally modified by a focused ion beam (Ga^+ source) to yield roughly 500 nm width gage section similar to a typical dog-bone shaped tensile test specimen. A total of three samples (PTP1, PTP2, and PTP3) were prepared in this way and the sample PTP3 was tested successfully. During the deformation process, the diamond indenter of the nanomechanical-testing device is moved against the PTP device's push knob. Force is measured

15   by the nanomechanical-testing device and the tensile displacement of the tensile sample is recorded using TEM image correlation. The measured average (N = 3 per device) spring force of the PTP device is subtracted from the force measurement to yield the force subjected on the sample during the test.

        All measurements were performed at ambient temperature prevailing inside the TEM with a

20   displacement-controlled nominal indenter speed of 1 nm/s. Once the pre-set value for full displacement is reached, the indenter was kept stationary for 3 - 5 seconds before returning to zero displacement with a nominal speed of 1 nm/s. The force and displacement were measured by a capacitive comb drive build into the testing device. During electron beam ON tests, the sample displacements were calculated from the combination of in situ TEM images using image

25   correlation and with capacitive measurement built-in to the nanomechanical-testing device. During electron beam OFF tests, the sample displacement was calculated using only the capacitive measurement built-in to the nanomechanical-testing device. Image correlation (LaVision ltd., DAVIS Software Suite v.8.3.1) was performed using a subset of 35 by 35 pixels and step size of 10 pixels. A high accuracy interpolation with 6th order spline functions were

30   used for the subpixel interpolation, whereas 2nd order nonlinear shape functions were used allowing more complex deformation of the subset. The displacements for the shear/compression experiments were obtained as the difference between the displacement of the lower part (diamond tool) and the upper part (sample), by selecting a region of interest from the diamond tool and the sample separately and exporting the displacements as an average of the selected

35   area. The displacements for the tensile experiment were obtained by tracking the movement of the edges of the tensile specimen using a Sobel Compass Edge detection algorithm. A manual image correlation was performed for some datasets to verify the digital image correlation results.

        The TEM magnification and associated electron flux was carefully selected not to induce crystallization (26) of the thin film samples during the "beam ON" tests. The test took

40   approximately 2 minutes for each shear/compression sample and approximately 12 minutes for the tensile sample. Alignment of the diamond tool with the thin film samples was conducted with negligible low electron flux. During the shear/compression test, the nominal TEM magnification was 87 000 X, and the electron flux was kept at $\sim$ 7.2 x 10^{21} e/m^{2}s. During the tensile test, the nominal TEM magnification was 10 000 X, and the electron flux was kept at $\sim$ 2.9 x 10^{19} e/m^{2}s.

45   These values correspond to approximate cumulative electron doses of 8.6 x 10^{23} e/m2 and 4.0 x 10^{22} e/m², respectively.

Measurement of the true stress

In nanomechanical testing, the raw measurement data is collected as force F $[N]$, measured by a force sensor. In order to understand what the mechanical loading capacity of the sample is, the force is converted into stress (pressure) σ $[N/m^2]$ in the sample as

$$\sigma = F / A \ , \tag{eq. S1}$$

where A $[m^2]$ is the measure of the contact area or cross-sectional area between the sample and the tool transmitting the force. True stress σ_t is defined as the instantaneous contact or cross-sectional area A_t under a load F

$$\sigma_t = F/A_t \ . \tag{eq. S2}$$

Instantaneous cross-sectional area of the tensile sample (PTP3) is calculated using TEM measured initial values: thickness 42 nm and width 560 nm. Tensile sample cross-sectional area is thought to be approximately a rectangle $t * w$, where t is the thickness [m] and w is the width [m] of the sample. During elastic deformation, w is measured to reduce by 2.14 %, which is divided for each measuring step to produce the true change in width. During plastic deformation the width changes linearly by 4.74 %, which is again divided linearly for each measuring step to produce the true change in width. The true thickness change is assumed to occur in equal percentage and the total changes are divided linearly for each measuring step.

Instantaneous contact area for the shear/compression samples is measured using x-axis and y-axis contact diameters defined in the nanomechanical testing setup (Fig. 1). The projected residual indent area left in the sample is measured to be elliptical in shape $A_{ellipse}$ by combining scanning electron microscopy (Zeiss ULTRAplus, Carl Zeiss AG), atomic force microscopy (AFM, Digital Instruments 3100, tapping mode) and in situ TEM imaging. The instantaneous true contact profile cross section is curved along the z-axis and the true contact area A_t for each sample is approximately $A_t = A_{ellipse} * 1.36$, which is estimated by AFM and in situ TEM data. During beam ON conditions, instantaneous contact diameter in the x-axis is measured directly from the in situ TEM images by digital image correlation. For the y-axis, the instantaneous contact diameter is measured as follows: the y-axis diameter of the residual indent is measured and then corrected by the elastic spring-back to yield the y-axis diameter at the peak load. The maximum diameter change is then divided linearly to each measuring step to produce the true change in y-axis contact diameter. Based on the FEM-simulations, here the σ_t corresponds to the average surface stress (pressure) over the entire contact surface, while the stress tensor exhibits a distribution within the deforming volume.

During beam OFF conditions, the x-axis and y-axis diameters are determined using the following process: The residual ellipse x and y contact diameters are measured and corrected using the elastic spring back to yield the contact diameters at peak load. The maximum diameter change is then divided linearly to each measuring step to produce the true change in contact diameters x and y. This approach of determining the contact area was verified to be valid using FEM modelling.

Measurement of the engineering strain

The strain is measured in engineering strain, as in the TEM, the glass does not naturally exhibit the contrast variations needed for true strain measurements related to the distribution of the strain tensor. Engineering strain is the measure of the relative deformation of a solid as

$$\varepsilon_E = \Delta l / l_0 \ , \qquad \qquad \text{(eq. S3)}$$

where $\Delta l \ [m]$ is the instantaneous total elongation of the solid and $l_0 \ [m]$ is the original length of the solid or the measuring gauge. In all experiments, the elongation $\Delta l = l - l_0$ is equal to the displacement measured along the z-axis of the nanomechanical testing setup (see Figs. 1A and 1B). In the compression and tensile simulations, the elongation is measured along the z-axis, while in shear simulations, the elongation is measured along the x-axis (see Figs. 1A and 1B)

In the tensile test setup, the instantaneous displacement is measured by image correlation. The l_0 was measured to be 2075 nm at the onset of fully elastic contact and the sample had a length of 2220 nm after the fracture (see Fig. 2A).

In the shear/compression test setup, the instantaneous displacement is measured using image correlation during beam ON conditions. In beam OFF conditions, the instantaneous displacement is measured using the capacitive measurement built into the nanomechanical-testing device. The capacitive displacement measurement is calibrated by using a known point where the sapphire and diamond tools come into contact. The engineering strain is then corrected using the calibrated capacitive displacement data. The l_0 was measured individually for the 14 samples tested in all imaging conditions. According to the FEM simulations, here the ε_E approximately equals the average engineering strain along the z-axis, while the strain tensor exhibits a distribution within the deforming volume.

Measurement of the viscosity

In the shear/compression tests, the definition of the shear viscosity can be used as the sample flows perpendicularly to the rigid tools used in the setup. We assume that the measured stress and strain rate are approximately equivalent to the shear stress and shear strain rate.

$$\eta_{shear} = \tau / \dot{y} \cong \sigma_t / \dot{\varepsilon}_E \quad , \qquad \qquad \text{(eq. S4)}$$

where η_{shear} is the shear viscosity, τ is the shear stress, $\dot{y}$ is the shear strain rate and $\dot{\varepsilon}_E$ is the engineering strain rate. In the tensile setup, we use the definition of extensional viscosity (44), in which

$$\eta_{extensional} = \sigma_t / \dot{\varepsilon}_E \ . \qquad \qquad \text{(eq. S5)}$$

For experimental viscosity plots presented in the study, we use the ratio of work of deformation and the active plastic volume $V_p \ [m^3]$ to calculate the viscosity. Force relates to the total work $W \ [J]$ done by the test geometry as

$$W = Fs \ , \qquad \qquad \text{(eq. S6)}$$

where $s \ [m]$ is the distance travelled under the load $F \ [N]$. Then the true stress related to viscous flow

$$\sigma_t = V_p/W \; , \qquad\qquad\qquad\qquad\qquad\qquad\qquad \text{(eq. S7)}$$

where the instantaneous active plastic volume is

$$V_p = C * l * A_t \; , \qquad\qquad\qquad\qquad\qquad\qquad\qquad \text{(eq. S8)}$$

where C is a correction factor. Correction factor $C = 1$ is used for the tensile tests. A correction factor $C = 4$ is used for the shear/compression, which is given by the finite element simulations indicating the real volume of stress field at yield stress related to the true contact area A_t under contact load. The ratio of active plastic volume and work is used, as we believe it better describes the strain rate dependent viscous behavior.

Finite element method modelling

Finite element method (FEM) modelling was conducted with the Abaqus software to verify the contact area measurements and estimate the active plastic volume in the shear/compression test setup.

Experimental measurements on the contact area indicated that the projected contact area of the residual indents have an elliptical shape with a ratio of approximatively 1.6 between the radiuses D1 and D2, which indicate that contact between the tip and the counter surfaces occurs with an elliptical contact geometry. In the simulations, the diamond tool counter surface was modelled as a cylindrical block with a thickness and radius of 150 nm and 320 nm respectively, so that one of the flat faces is the contact surface. The sapphire tip was modelled by sweeping an arch with a radius of R1 along the secondary arch with a radius of R2. Hence, the shape of the tip had a double curved surface. The radius R1 corresponds to the experimentally measured tip radius of 96 nm. R2 radii can vary from sample to sample, and therefore, different R2 radii were used to study its effect on the resulting plastic volume. The height of the tip was 270 nm. The tip was divided into two sections so that the 60 nm thick top layer could be given different material properties than the bulk of the tip, thus representing the thin film specimen. The model utilizes a symmetry in two planar axes' so that only a quarter of the geometry was modelled.

The element used for the thin film specimen was a linear hexahedron with hybrid formulation (C3D8H), which is suitable for simulating large strains. Standard linear hexahedron elements (C3D8) were used in the diamond counter surface. The element size varies in the model but was approximately 7 nm at the contact, though 5 nm and 10 nm mesh sizes were utilized to verify that the element size was sufficiently small. The simulation used adaptive re-meshing rule (ALE) to cope with large mesh distortion due to large plastic deformation.

Symmetry boundary conditions were applied to the symmetry planes of the model. The bottom surface of the tip and the top surface of the counter surface were coupled to two separate reference points. Initially all degrees of freedom for the two reference points were set to zero, and the test was then simulated by moving the reference points towards each other in a linear fashion in a single load step with 40 calculation increments with the setting for the non-linear geometry set as active (Nlgeom). Contact between the tip and the counter surfaces was modelled using standard "hard contact" formulation in normal direction, and the contact was frictionless.

The diamond counter surface and the bulk sapphire tool were given linearly elastic material properties without plasticity. The specimen on the surface of the tip was given elastic-plastic material model following an isotropic hardening rule (von Mises). The elastic-plastic mechanical

behavior model was adapted from the current molecular dynamic simulations results of this study and from literature (*16*). **Table S1** lists the elastic moduli and Poisson's ratios for the compression tools and for the sample film, whereas **Table S2** lists the FEM parameters for the plastic part of the mechanical behavior model.

5

Supplementary Text

S1. A tool to measure unconfined mechanical response of thin films in situ in TEM

Figure S1 shows a 3D model of a sapphire tool deduced from a tomography experiment performed using the scanning transmission electron microscopy in high angle annular dark field imaging mode (STEM-HAADF). The sapphire tool is specifically designed for in situ mechanical testing of thin films. The tool was designed with a similar concept to what was used by Minor et al. (*45*), but with a substrate material suitable for hard material testing. The benefit is that a thin film deposited on the tool is electron transparent and ready to be tested as received. Therefore, the films undergo no manipulation after deposition (such as ion beam milling), which could change their mechanical properties and behavior. Tools are manufactured using a combination of Angled Broad ion beam Milling "ABeaM" technique with a broad ion beam (Ilion II, Gatan Inc.) and focused ion beam milling (Zeiss crossbeam 540, Carl Zeiss AG). Concerning this study, a total of 84 anvils were produced and coated with a thin film.

S2. TEM characterization of the in situ experimental samples

Figure S2 shows in situ electron diffraction images of an a-Al_2O_3 film at $t = 0\ s$ exposure (**Fig. S2A**) and at $t = 120\ s$ exposure (**Fig. S2B**) to a condensed electron beam in TEM. The as-deposited films appear amorphous and start to crystallize after a critical dose of electron beam. Crystallized areas can be easily distinguished from the amorphous material by diffraction contrast (**Figs. S2C** and **S2D**). Because of this behavior, the electron dose during beam ON conditions was carefully selected not to induce crystallization of the samples. Finally, no crystallization was detected in situ or ex situ in any of the samples mechanically tested with beam ON conditions.

Although the as-deposited films appear predominantly amorphous, low concentration (approximately $0 - 10$ crystals per $10\ 000\ nm^2$) of nanocrystals (approximately $4 - 10$ nm diameter) can be detected in the as-deposited films by diffraction contrast and high-resolution imaging. Because of this inherently low concentration, no crystals were detected in the sample volume subjected to plastic deformation, and therefore, the experimental results represent the mechanical behavior of fully amorphous aluminum oxide. **Fig. S3A** shows a rare case of a shear/compression sample with nanocrystals. However, in this case, the crystals reside outside the deformation volume, while the rest of the sample is amorphous. **Fig. S3B** shows a high-resolution image of an individual nanocrystal, giving proof of its crystallinity.

A minor carbon contamination layer is most likely formed on the sample surface due to prolonged electron beam exposure during mechanical tests. However, the effect on the measured force is assumed negligible, as the strength of such a contamination layer will be significantly lower compared to the stress needed to flow the sample.

S3. In situ experimental and simulation stress/strain data of amorphous Al_2O_3

In all cases, a-Al_2O_3 exhibits first a non-linear elastic response before reaching the yield stress and flow of the material. In **Fig. 2A**, a small mismatch in the tensile elastic property results

of simulations and experimental stem from the profound difficulty of performing an experimental tensile test without a shear component. **In Fig 2B**, the larger mismatch between the elastic properties of the simulated and experimental shear/compression emerges because of two main reasons: first, the experimental loading curve in **Fig. 2B** is a combination of shear and compression loading, which explains the overall low measured elastic modulus, whereas in the simulations the loading is pure compression or pure shear. Secondly, specifically the early stage elastic mismatch in **Fig. 2B**, originates from the difficulty of obtaining the true contact area during the first moments when the tool and the specimen come in contact with each other.

Figure S4 shows all the individual experimental measurements used to produce the average experimental shear/compression results. We experimentally tested the shear/compression behavior both without (Beam OFF, **Fig. S4A**) and with (Beam ON, **Fig. S4B**) electron beam and found that there is no large difference in the flow behavior. The possible change in flow stress caused by the electron beam cannot be detected beyond the normal deviation of the average results. Nominal displacement rate is 1 nm/s, however the displacement rate fluctuates dynamically during all the tests, which also leads to changes in the strain rate and the measured flow stress. **Fig. S5** shows all the individual simulations used to produce the average results. The strain rate is fixed for a given plot as indicated in the figure legend. In addition, **Fig. S5A** shows how the pressure in the tensile simulations is released back to atmospheric pressure four times, which indicates that permanent deformation occurred throughout the flow stress region.

S4. Void and crack evolution in the tensile sample

Figure S6A shows a void nucleating inside the tensile sample towards the end of the tensile test (0.14 strain). The void then evolves into a sharp edge crack (**Figs S6B, S6C**) and propagates further until it reaches the critical length (**Fig. S6D**) leading to fracture of the sample immediately after. The nucleating void and the subsequent edge crack are relatively stable as it takes 23 s with the nominal pulling speed of 1 nm/s to reach the critical crack length of 135 nm.

S5. Effect of sample preparation on the mechanical behavior of a-Al_2O_3

In situ TEM samples used for the shear/compression studies are directly deposited on the tool. Therefore, the samples are considered to be in the as-deposited state at the beginning of the experiment. However, the tensile test requires a two-step preparation as introduced in the methods section. The focused ion beam preparation is found to modify the milled edges of the sample and STEM + EDS mapping reveals clusters of gallium near the milled edges as shown in **Fig. S7**.

Interestingly, we find that the void nucleating in the tensile experiment occurs inside this damaged area, and during the viscous flow, the void grows and transforms into a sharp edge crack. **Fig. S8** shows the tensile sample after fracture and the location of the void nucleation.

We believe that the point defects created by the highly energetic ion beam start to coalesce during the plastic deformation phase. The coalescing defects eventually form a void, which then propagates to form an edge crack, which further propagates until it reaches the critical crack length of 135 nm, after which a brittle fracture occurs. It is possible that without the ion milling preparation, the void nucleation could be prevented or significantly slowed down and a much higher tensile strain could be reached as indicated by the atomistic simulations.

S6. Plasticity mechanisms in a-Al_2O_3

The momentary ($\Delta\varepsilon = 0.01$) distribution of D^2_{min} in **Fig. S9** clearly shows localization of the plastic strain, shown as blue areas in the simulated structures. The fluctuations of stress during a single simulation can be directly correlated to the localized plastic deformation events as shown in the **Fig. S10**, i.e. large increase in the momentary atom movement results in decrease of stress and vice versa. As shown in the **Fig. S11**, over a cumulative compressive strain ($\Delta\varepsilon = 0.5$) these localized plastic deformation zones vary and the cumulative plastic strain is randomly distributed to produce an overall homogenous plastic flow. In comparison to the D^2_{min} descriptor, the mean square displacement (MSD) shown in **Fig. S12** poorly captures the real strain distribution of the cumulative plastic deformation.

S7. Electron beam induced temperature increase during in situ TEM experiments

Nakamura et al. (*26*) studied TEM electron beam heating in amorphous Al_2O_3 thin films and found that the thin film theoretically heats up by only a few Kelvins during electron irradiation. Following the calculation method by Nakamura et al., the maximum temperature increase during TEM electron beam irradiation can be estimated as

$$T_{max} = W_0[1 + 2\ln(R/r_0)]/4\pi l_0 k \quad , \tag{eq. S9}$$

where R $[m]$ is the radius of the sample holder grid hole in which the sample is held, r_0 $[m]$ is the radius of the irradiated region, l_0 $[m]$ is the sample film thickness, k $[Wm^{-1}K^{-1}]$ is the thermal conductivity of the sample film, and the total absorbed power $[W]$ of the electron beam is

$$W_0 = \varphi V \rho_0 \pi r_0^2 \quad , \tag{eq. S10}$$

where φ [ ] is the fraction of energy absorbed from the electron beam, V $[V]$ is the acceleration voltage and ρ_0 $[Am^{-2}]$ is the beam current density. **Table S3** summarizes the calculations for the shear/compression and tensile experiments.

In addition, Nakamura et al. report an experiment, in which indium nanoparticles placed on an amorphous Al_2O_3 thin film sample cannot be melted together when irradiated by electrons in TEM. This indicates that the temperature increase in the film is below the melting temperature of bulk indium ($T_m = 430$ K), which verifies that the temperature during in situ experiments is well below the glass transition temperature of a-Al_2O_3 (bulk $T_g \sim 973$ K (*25*)).

S8. Adiabatic heating during the in situ experiments

As the flow stress is high, we can expect a strong adiabatic heating effect during plastic deformation, as given by the Taylor-Quinney relation for plasticity-induced heating. However, the obvious should be pointed out: the generation of heat during plastic deformation takes place only after yielding, which demands that the sample remains very close to ambient temperature at the onset of plastic flow.

A calculation using the Taylor-Quinney factor gives the order of magnitude for the potential plasticity induced adiabatic heating in a solid (*46*).

$$\Delta T = \frac{\beta}{\rho c} \int_0^\varepsilon \sigma \, d\varepsilon \quad , \tag{eq. S11}$$

where β [ ] is the Taylor-Quinney factor (factor by which plastic work is transformed into heat), ρ $[kgm^{-3}]$ is the density of the solid, C $[Jmol^{-1}K^{-1}]$ is the heat capacity, ε [ ] is the strain, and σ $[Pa]$ is the stress. We can assume that at room temperature, $\beta = 0.6 - 0.95$, $\rho = 3325\ kgm^{-3}$, $C = 72.3\ Jmol^{-1}K^{-1}$ ($T = 273.15$ K, $\alpha - Al_2O_3$ (47)), and $\sigma = 4.8 * 10^9\ Pa$. Then for each plastic strain step of $\varepsilon = 0.01$ the maximum potential temperature increase would be 120 - 190 K. When compensated with thermal conductivity, the real temperature change will be less, as our experimental strain rates are considered to be quasi-adiabatic. Moreover, as we do not detect heat-induced crystallization during plastic deformation, the temperature increase has to be substantially lower. This shows that due to the large stress level in the sample, adiabatic heating could very well influence the oxide glass mechanical behavior after yielding, especially at higher strain rates.

S9. Effect of electron beam on the mechanical response of a-Al$_2$O$_3$

To further study the electron beam effect on the mechanical behavior of a-Al$_2$O$_3$, we performed a dedicated "beam-ON / beam-OFF" mechanical test, in which the electron beam is switched OFF during the steady state viscous creep of the a-Al$_2$O$_3$ thin film. Results show (**Fig. S13**.) that in the event of beam switch-OFF, the flow stress level does not change enough to be interpreted to occur outside the normal stress fluctuation caused by the dynamic strain rate.

S10. Fracture toughness and the size effect

It is possible to induce plasticity by dramatically increasing the ratio of surface atoms to bulk atoms. Using the in situ approach, we can directly observe whether the resistance to fracture has artificially improved via a possible sample size effect. Using the Griffith's criterion (*11*), we can estimate the critical stress intensity factor K_{Ic} in tension for a-Al$_2$O$_3$ by using the measured critical crack length of 135 nm (**Fig. S6**) and the highest measured stress value

$$K_{Ic} = \sigma\sqrt{\pi c} = 4800\ MPa\sqrt{3.14 * (135 * 10^{-9}\ m)} = 3.1\ MPa\sqrt{m}\ . \qquad \text{(eq. 12)}$$

The measured K_{Ic} is in good agreement with the typically measured critical stress intensity factors for bulk (crystalline) Al$_2$O$_3$ ($K_{Ic} \sim 2.0 - 6.0\ MPa\sqrt{m}$). As the plastic deformation mechanisms activate, the material appears to achieve higher "toughness" or resistance to cracking, but the key property is the full absence of critical flaws as also indicated by the atomistic simulations performed in parallel.

S11. Replicating a-SiO$_2$ simulation setup performed by Luo et al. (*24*) using a-Al$_2$O$_3$

We compared our atomistic simulation setup to a literature setup by Luo et al. (*24*) on a-SiO$_2$, where a-SiO$_2$ exhibits brittle fracture after $\sim$ 15 % total tensile strain with periodic boundary conditions. We replicated the simulation setup (simulation cell size, strain rate etc.) of Luo *et al.*, which more than doubles the simulation cell size along the tensile axis for a-Al$_2$O$_3$ and we observed no fracture up to 30 % tensile strain.

Here, the same cell size and strain rate were used as described by Luo et al. First, three structures of 200 x 100 x 100 Å were created by joining two 100 x 100 x 100 Å structures that were equilibrated at 3000 K into a right square prism shape so that the long direction of the structures were along X, Y, or Z axis. The resulting structures were equilibrated further at 3000 K for 45 ps in NVT conditions using periodic boundary conditions (PBC), cooled to 650 K with cooling rate of 3.61 K/ps, and equilibrated at 650 K for 35 ps. The desired 110 x 55 x 55 Å

structures were cut from these, and equilibrated at 300 K for 100 ps in NVT with periodic boundary conditions. The densities were allowed to relax by simulating structures with barostat bringing directional pressures to zero over 100 ps, and additional 300 ps of NPT simulation at zero pressure.

In the strain simulations, a constant strain rate of 1 x 10^9 1/s was applied along the 110 Å dimension of the cell, and barostat was used to keep the lateral directions at ambient pressure. Strain simulation duration was 300 ps, and the structure was strained by 30 %. No fracture was observed in any of the three simulations. The flow stress shown in **Fig. S14** is similar to the flow stress in the original 50 Å cubic cell simulations, in which there is a slight trend towards higher stress at higher strain rates. Bond exchange statistics and coordination number distributions were practically identical to the original simulation results.

Moreover, **Fig. S15** shows that the fractions of increased / decreased / swapped coordination at 0.15 strain in a-Al_2O_3 are 13 % / 17 % / 21 %, respectively, whereas a-SiO_2 has 0.5 / 2 % / 1 % (*24*). This gives the difference of approximately 8 - 25 times in the propensity to change the coordination or bonding between present work and a-SiO_2 in the Ref. (*24*). In addition, it is important to note that the simulated a-SiO_2 fractures after 0.15 strain. Therefore, the difference in the compared values is not caused by the fracture.

The blue and black datasets in the **Figs. 4B and S15** appear to start from 3 – 4 % fraction. This is because we saved the trajectory at a rate of 1 structure every 1 ps. This was verified by performing additional short simulations with the same initial structure and velocities, and with trajectory saved every fs. In these simulations, the number of atoms with increased/decreased CN starts from zero, as expected, and rises to ~ 3 – 4 % within 200 fs. This is observed with strain, and also in the non-strained NPT simulations, which indicates that the change is simply due to the alumina's propensity to bond switching and thermal vibrations. The saturation could be due to thermal vibrations stochastically moving atoms in-and-out of the cut-off radii of their neighbors so there is no continuous uniform movement.

S12. The effect of the simulated quenching procedure to the a-Al_2O_3 mechanical behavior

To study the effect of quenching methods on the stress-strain behavior of a-Al_2O_3, we performed additional simulations using a "cast-quenched" starting structure. This structure was obtained by taking the original cut starting structure, heating it up to 3000 K and repeating the same equilibration and cooling sequence as before using periodic boundary conditions. This included equilibration at 3000 K for 45 ps, cooling to 650 K over ~ 650 ps at the rate of ~ 3.61 K/ps, and equilibrating it for a total of 500 ps at 300 K, of which 100 ps was with NPT to relax the simulation cell to a stress free state.

Bond lifetime analysis of unstrained simulations at 300 K shows that bond interchange is too slow to properly equilibrate the cut edges. The high-coordinated environments are slightly more common in the cast-quenched starting structure even though all local environments that are present in cast-quenched starting structure are present in the original starting structure and vice-versa. Notwithstanding, there is probably a different distribution of local environments at the cut edges, or different bond angles that affect the behavior in strain simulations, because they behave slightly differently under strain.

The overall simulated mechanical behavior with the cast-quenched structure remains very similar: the material yields plastically, the flow stress measured between 25 – 30 % strain (as in **Figs. 1C** and **3B**) saturates to same magnitude as in the original quenching procedure and no fracture is observed at any strain rate (**Fig. S16**). In addition, we simulated a larger cast-

quenched structure as in the supplementary section S11 and again observed no fracture under tension. Therefore, all the conclusions related to the plasticity and viscosity remain unchanged.

The most notable change is that the simulated non-linear elastic yield stress (peak stress) increases by 1 – 1.5 GPa (20 – 30 %) depending on the strain rate suggesting that the bulk initially becomes stronger when using the casting quench method. We found that this increase in yield stress is related to the time-dependent nature of the mechanical behavior as the difference in strain rate between experimental and simulated tensile test is $\geq 1 \times 10^{10}$ (1/s). In fact, the peak stress tends to decrease with decreasing strain rate (**Fig S17**), and if the trend continues to experimental strain rates, the peak stress could approach experimental stress levels. This suggests that also the non-linear elastic properties of a-Al_2O_3 have a time-dependent nature, as should be expected (*22*).

S13. Cavities in the atomic structure of a-SiO_2 and a-Al_2O_3

The atomic structure of a-SiO_2 has large amounts of cavities or free volume (*29, 30*), which spatially inhibit bond switching from occurring in tension, and could act as a critical flaw initiating fracture (*32*). **Fig. S18** shows the cavity volumes calculated for the atomic structures of a-Al_2O_3 (**Fig. S18A**) and a-SiO_2 (**Fig. S18B**), respectfully, by using the surface-based cavity definition in pyMolDyn (*42*). Although, a-SiO_2 can appear flaw free in TEM images (*24, 27*), the random porosity of the a-SiO_2 atomic structure would not be easily distinguished by the contrast formation in TEM and can easily lead to the premature conclusion that the sample is free of geometrical flaws.

S14. Activation energy of viscous creep

Activation energy of viscous creep is measured using the experimental data on work over active plastic volume for both shear/compressive and tensile experiments. The reported value is an average and error is given in standard deviation. The effective activation energy of the glass structure is calculated by dividing the total instantaneous work W by the number of ions N_{ions} flowing in the instantaneous active plastic volume V_p

$$Q_{eff} = W/N_{ions} \ . \qquad\qquad\qquad\text{(eq. S13)}$$

For calculating the amount of ions in the active plastic volume, we use density $\rho(a-Al_2O_3) = 3.255 \ gcm^{-3}$, given by the molecular dynamic simulations. Data used to calculate the average and standard deviation is combined from both tensile (PTP3) and shear/compression (3.1 and 3.4) samples. The "effective" activation energy is used as the definition since activation energy of the disordered glass structure likely has a wide distribution and the effective energy can be defined as a mean value of that distribution. This is in comparison to crystal lattice activation energy, which has certain activation energy quantums in different crystallographic orientations.

S15. Characterization of simulation structures

The pair correlation function, g(r), is very similar across all simulations. As seen in the **Figs. S19**, **S20**, **S21** and **S22**, there is little to no difference in g(r)'s before and after straining. The first Al-O peak is well separated from Al-Al and O-O peaks, so it is possible to choose 2.25 Å as a cut-off for bonded atoms, and this cut-off is used throughout the study. The only differences between tensile and compressive simulations is that the latter has a slight (~ 0.1 Å)

shift in the Al-Al and O-O peaks towards lower radii. As this is at higher r than the cut-off at 2.25 Å, it does not affect the choice of the cut-off.

The distribution of coordination numbers changes slightly (± 5 % in tensile, ± 10 % in compression simulations) early in the simulations during the first 5 – 10 % of strain. The change correlates with the density change, and it is likely that they are related. After this initial change, there are slight variations of up to ± 5 % change later on in some simulations but there is no trend-like change. Examples of the simulations with these variations are shown in **Figs. S23 and S24**. In tensile simulations shown in **Fig. S23**, 3-coordinated O and 4-coordinated Al make up 70 – 80 % of the respective elements, 2-coordinated O and 5-coordinated Al make up 15 – 25 % of the respective elements and 4-coordinated O and 6-coordinated Al make up less than 5 %. In compression simulations shown in **Fig. S24**, the coordination numbers change to the opposite direction in the early simulation, and afterwards settle at 55 – 60 % of 4-coordinated Al, 30 – 40 % of 5-coordinated Al, and 5 % of 6-coordinated Al. Oxygen coordination settles at 80 % of 3-coordinated O, and 10 % of both, 2-coordinated and 4-coordinated O.

In both, tensile and compression strain simulations, the Al-centered polyhedra were readily visible from angle distribution of Al-atoms with four or six nearest neighbors. The angle distributions matched closely to those of tetrahedral or octahedral bond orientation, so the number of Al-centered tetrahedra and octahedra is essentially equal to the number of 4-coordinated   or 6-coordinated Al. 6-coordinated oxygen did not exist in any meaningful quantities, so there are no O-centered octahedra. However, 4-coordinated O did exist, and analysis of the angular distribution of bonds shows two peaks centered at ~ 90 ° and ~ 115 °. A closer look at 4-coordinated O shows mostly polyhedra-type structures regardless of the angles. Most such O have some Al-neighbors forming Al_2O_2 square units, which causes the peak at 90 ° bond angles, and some not forming squares, which causes the peak at higher angle. A relatively low number of planar bond orientations were found. These form when all four Al atoms around a single oxygen are interconnected with square structures.
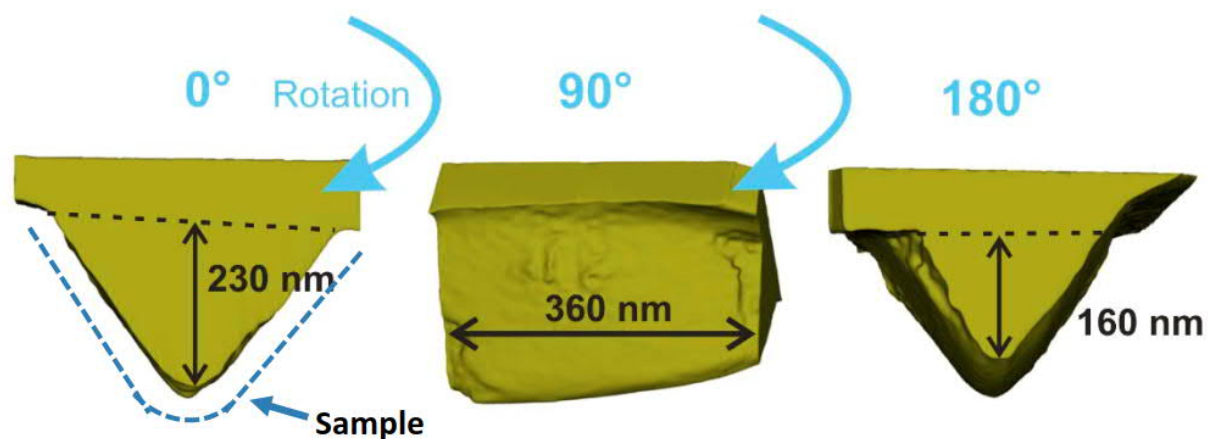
Fig. S1.

A 3D model of a STEM-HAADF tomography showing the general dimensions and shape of the used shear/compression sapphire tool for in situ TEM.

5
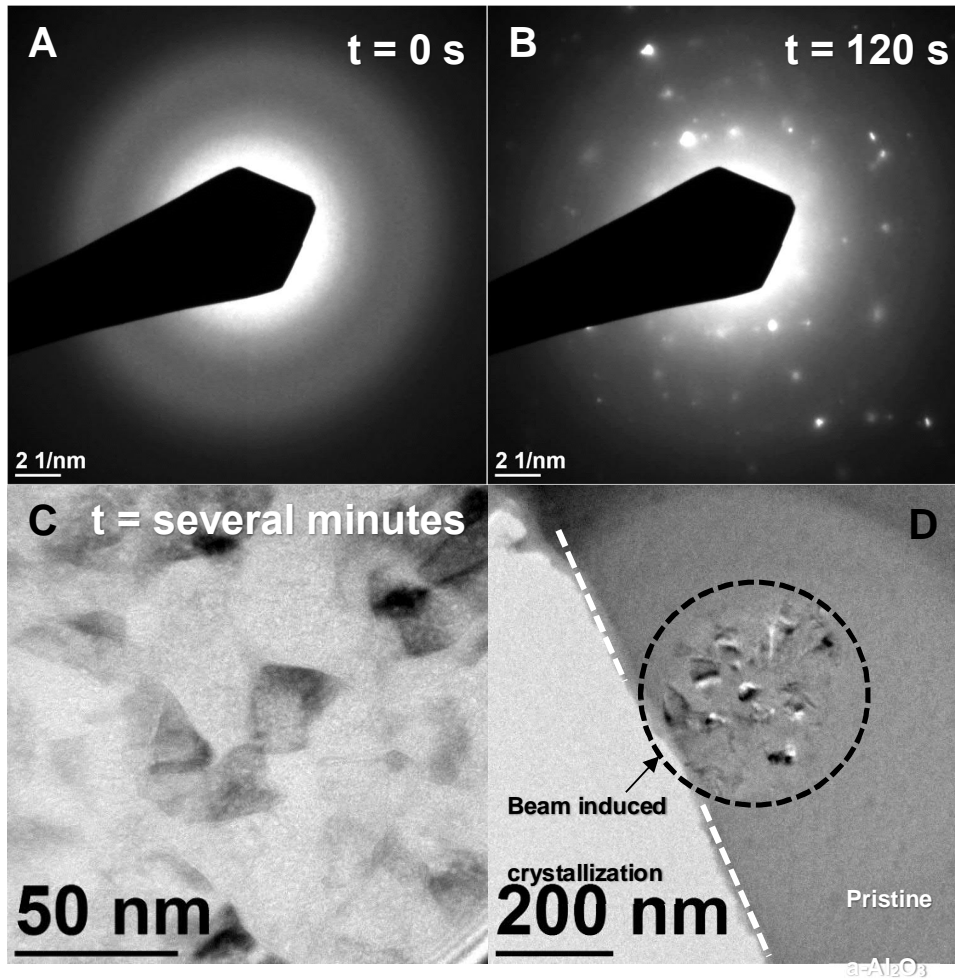
Fig. S2.

TEM electron diffraction on the as-deposited a-Al_2O_3 thin films. (A) t = 0 s, showing amorphous
rings (B) t = 120 s, showing a spot pattern indicating a partial transition from amorphous to
crystalline structure (C) bright field image showing diffraction contrast from several electron
beam induced nanocrystals of Al_2O_3 (D) Lower magnification image showing the contrast
difference between an area crystallized by the electron beam and the surrounding pristine a-
Al_2O_3.
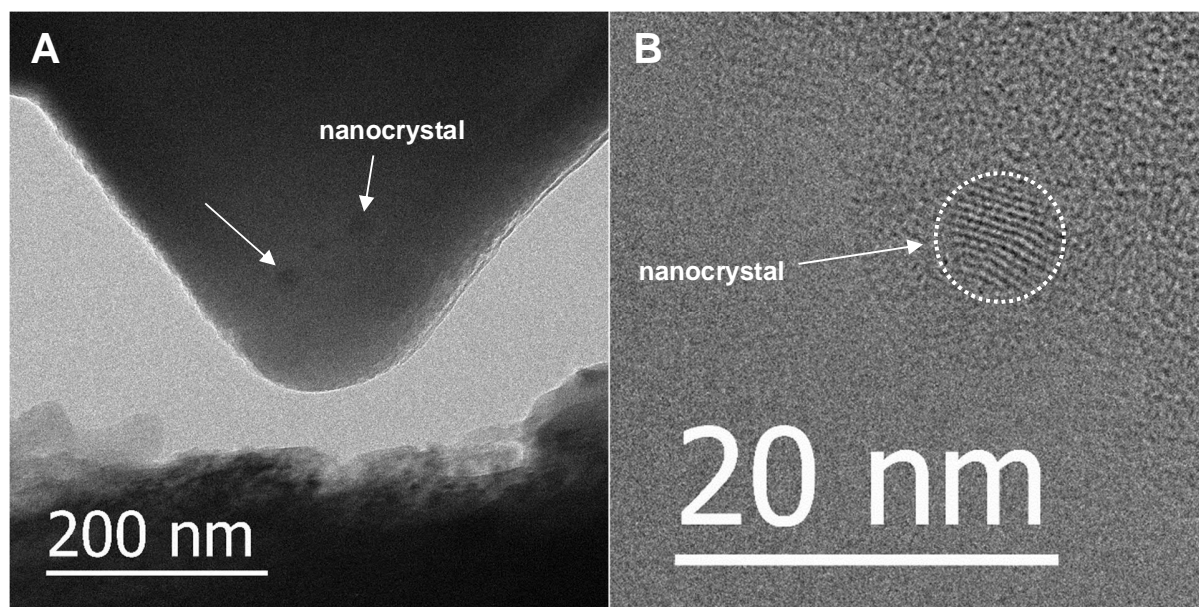
Fig. S3.

Observations of rare nanocrystals residing in the as-deposited a-Al$_2$O$_3$ films. (A) Single nanocrystals detected in the sample 2.3 and (B) a high-resolution image of an isolated nanocrystalline domain in amorphous matrix showing regular lattice fringes.
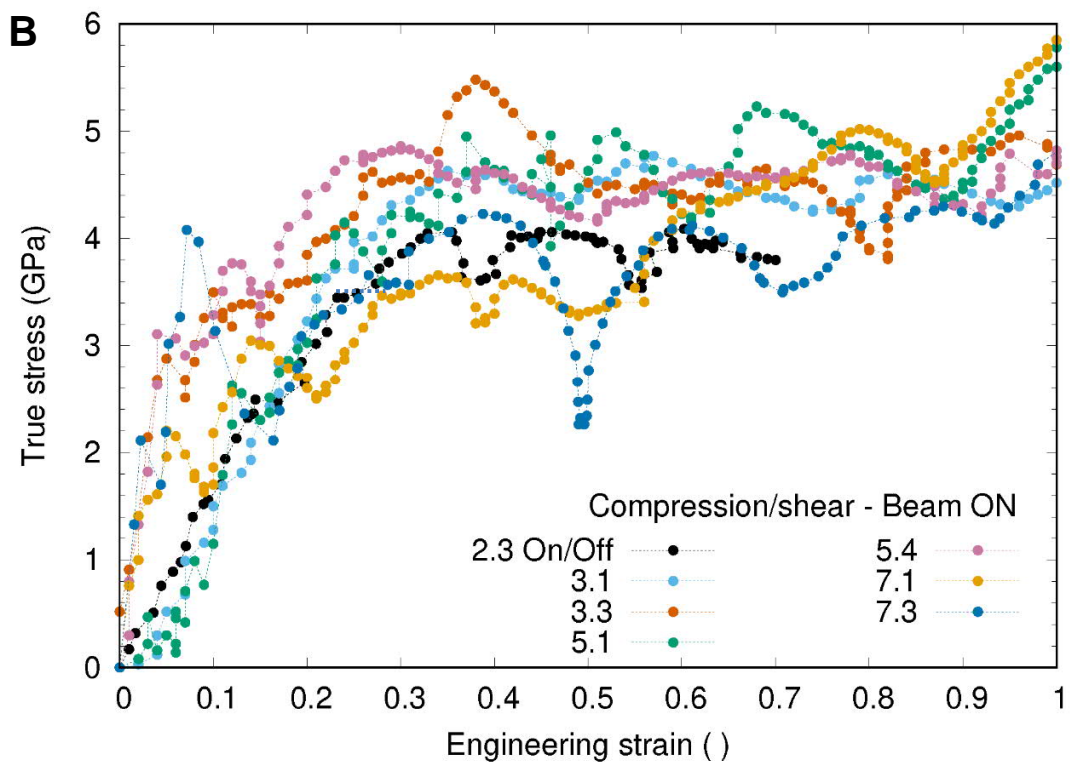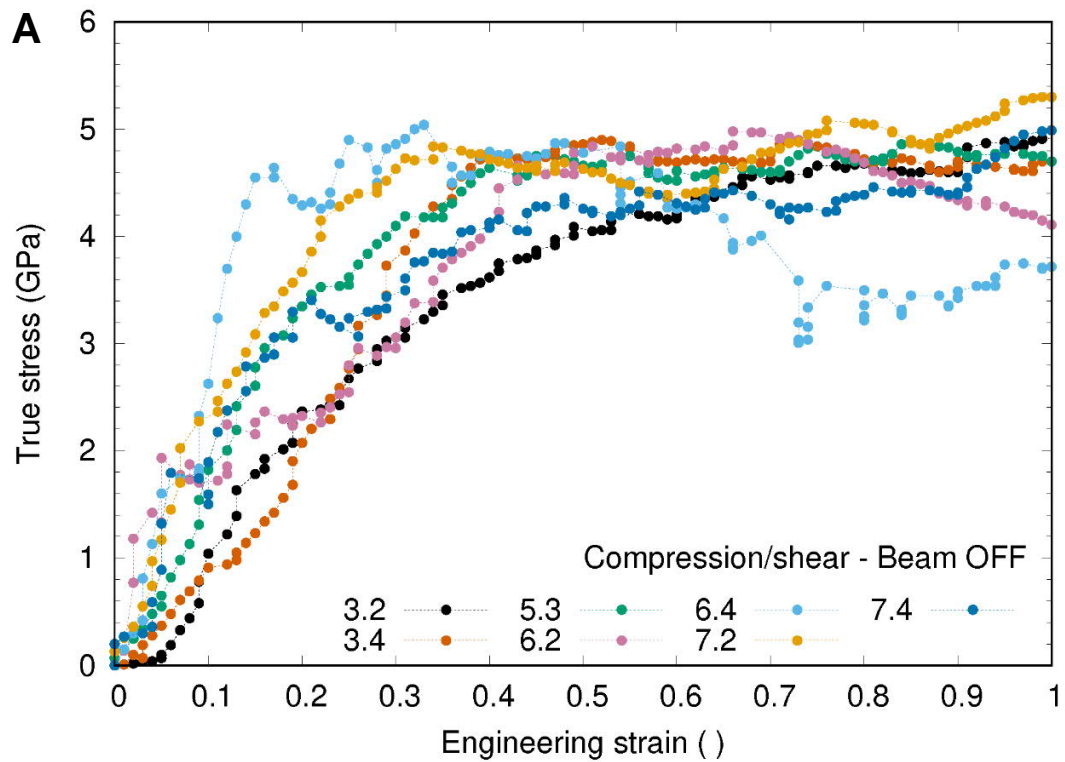
Fig. S4.

Results of the individual in situ TEM shear/compression experiments. (A) Results with the electron beam switched OFF during the experiments (N = 7) and (B) the results with the electron beam switched ON during the experiments (N = 7). The strain during the beam ON tests is calculated using image correlation, while the strain in the beam OFF tests is measured with the built-in capacitive transducer. In the x.y. sample labelling, x is the number of the tool batch and y is the number of individual tool in that batch.

5
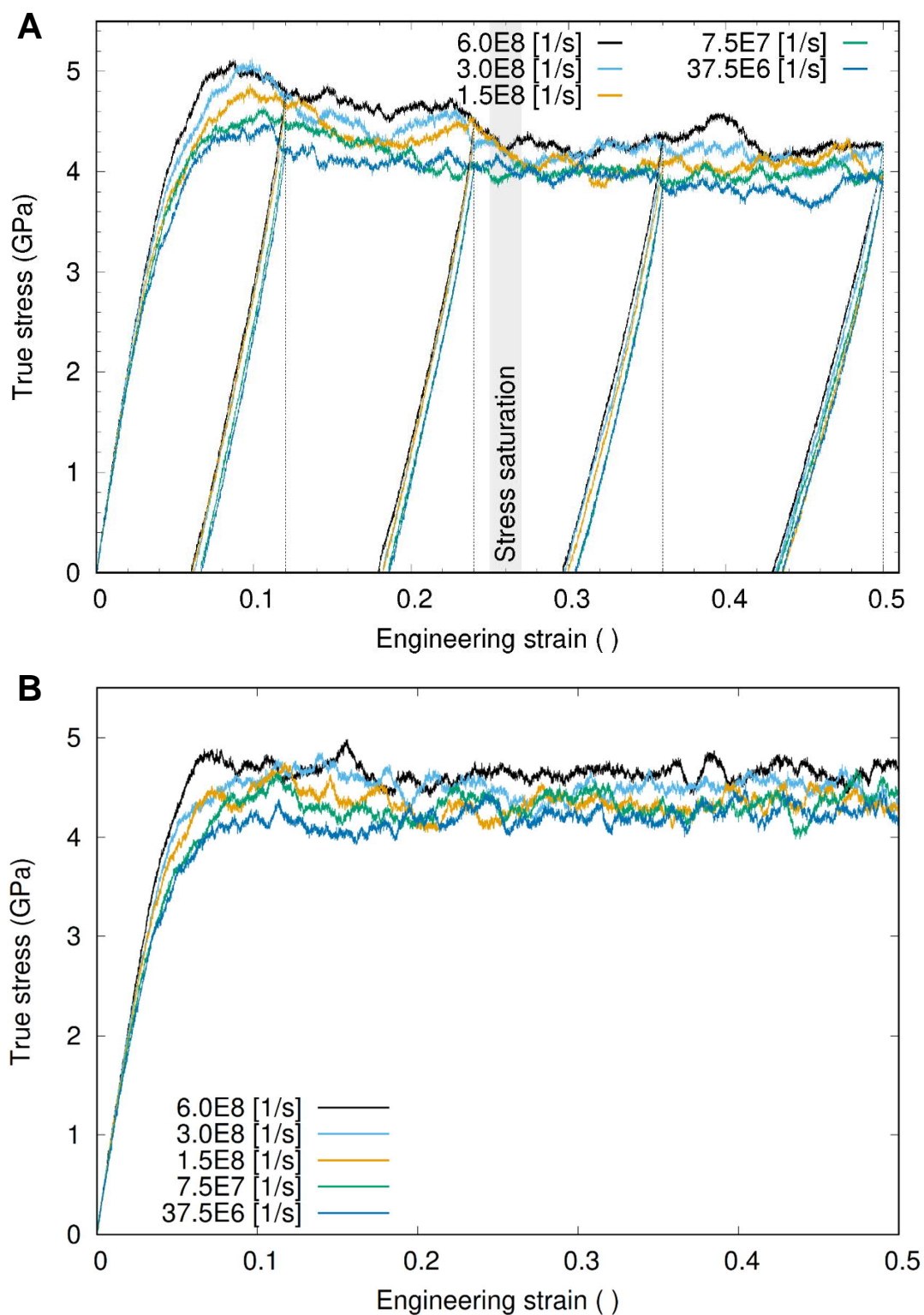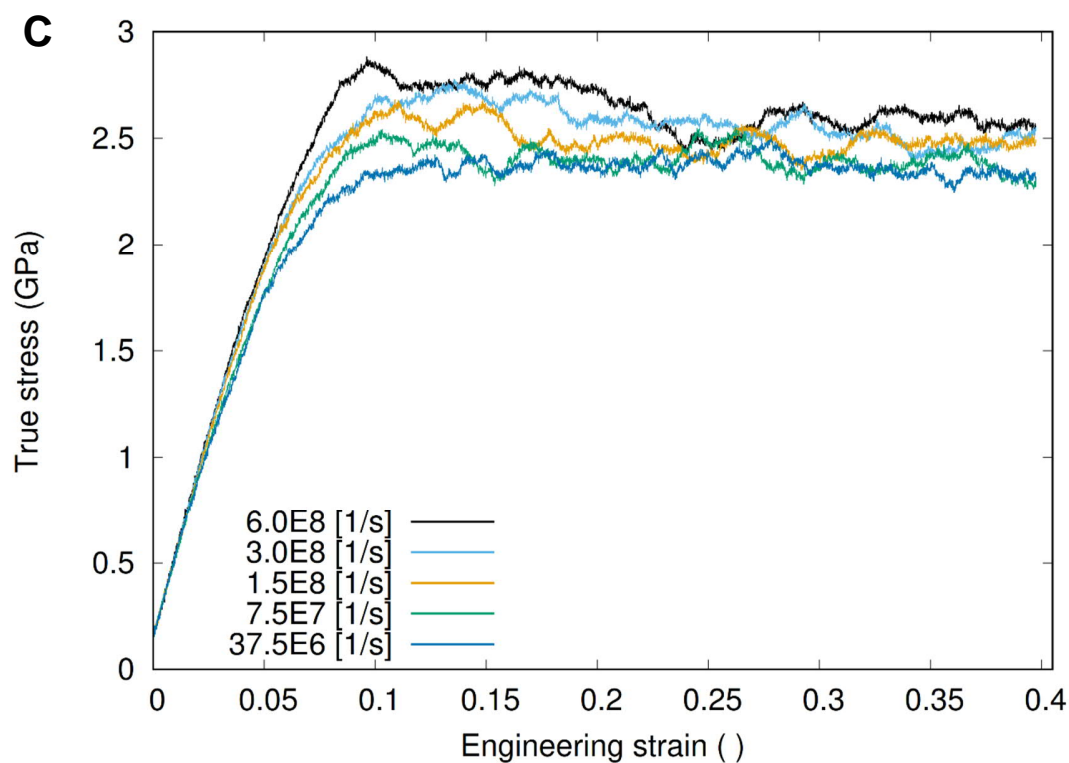
Fig. S5.

Averaged simulated mechanical behavior of a-Al$_2$O$_3$ with different strain rates. (A) In tension, released to atmospheric pressure 4 times and dashed lines indicate the release points (N = 6), (B) In compression (N = 6), and (C) In shear (N = 6). Temperature set to 300 K.
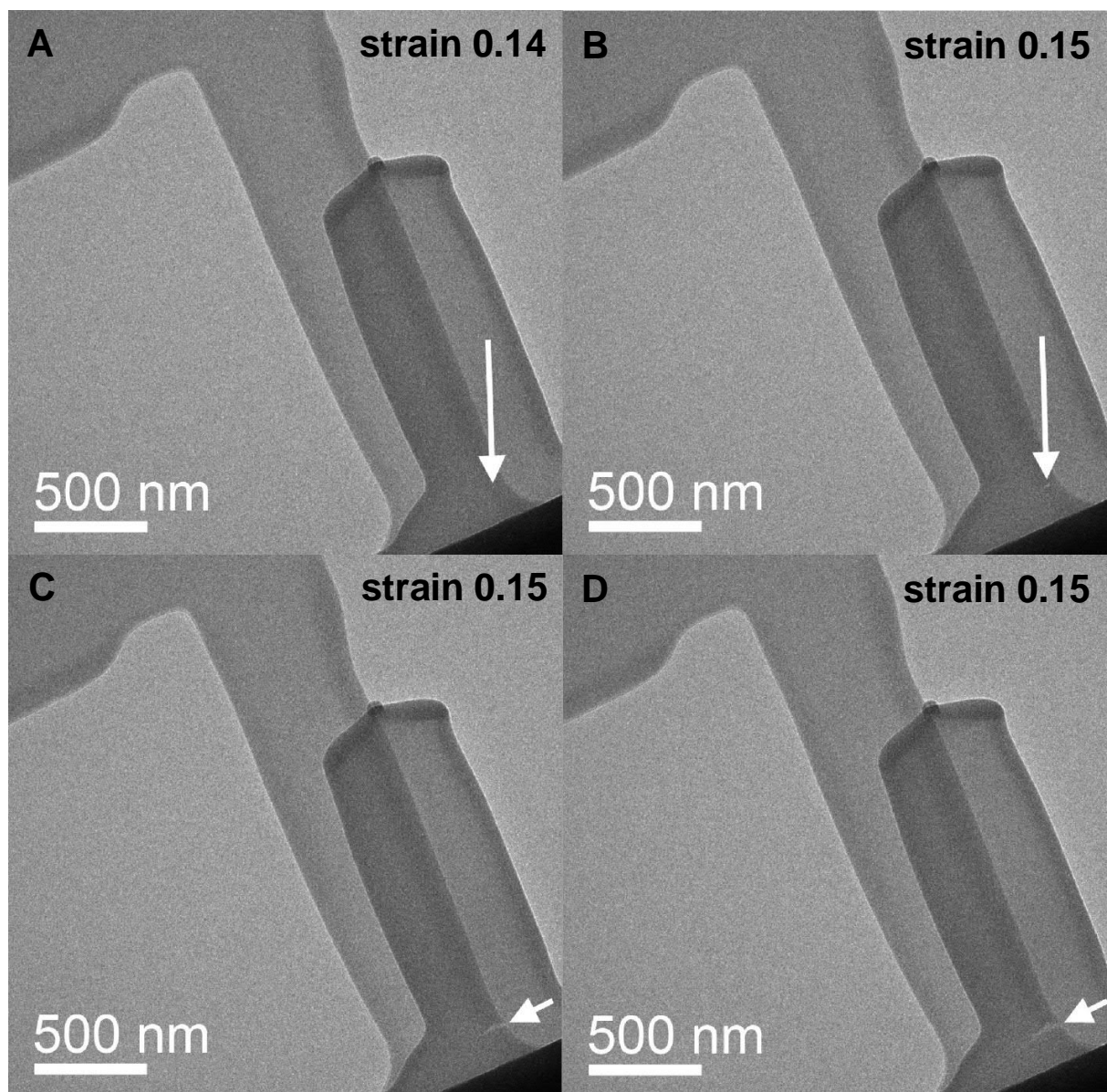
Fig. S6.

Void and edge crack evolution in the in situ tensile test. (A) Void nucleation and (B) growth, (C) transformation into a sharp edge crack, and (D) propagation to the critical length (135 nm). Strain related to the stress/strain data is marked in each image.
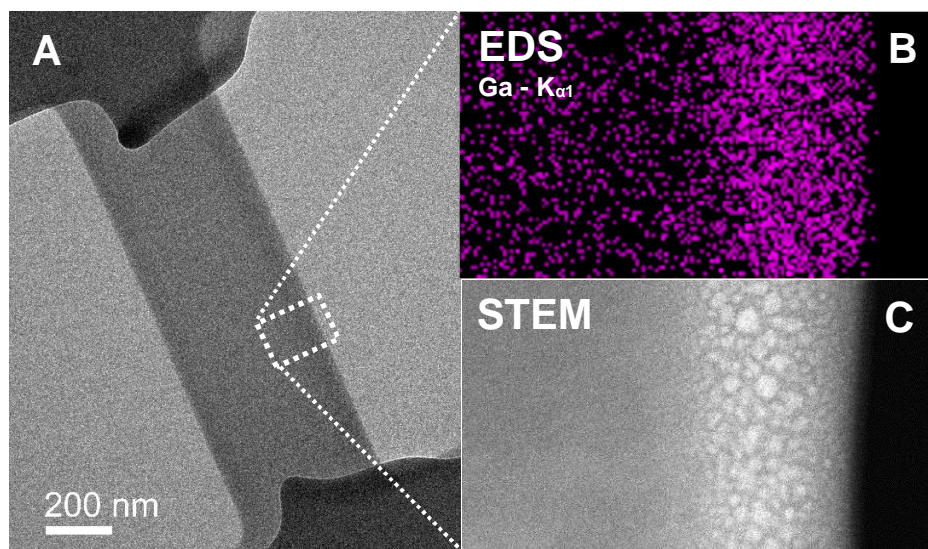
Fig. S7.
Effects of the focused ion beam milling on the in situ tensile sample. (A) A general image of an a-Al_2O_3 tensile sample. (B) Element mapping reveals that the milled edge has an elevated concentration of gallium. (C) STEM image showing that the milled edge contains clusters of heavier elements than aluminum and oxygen.
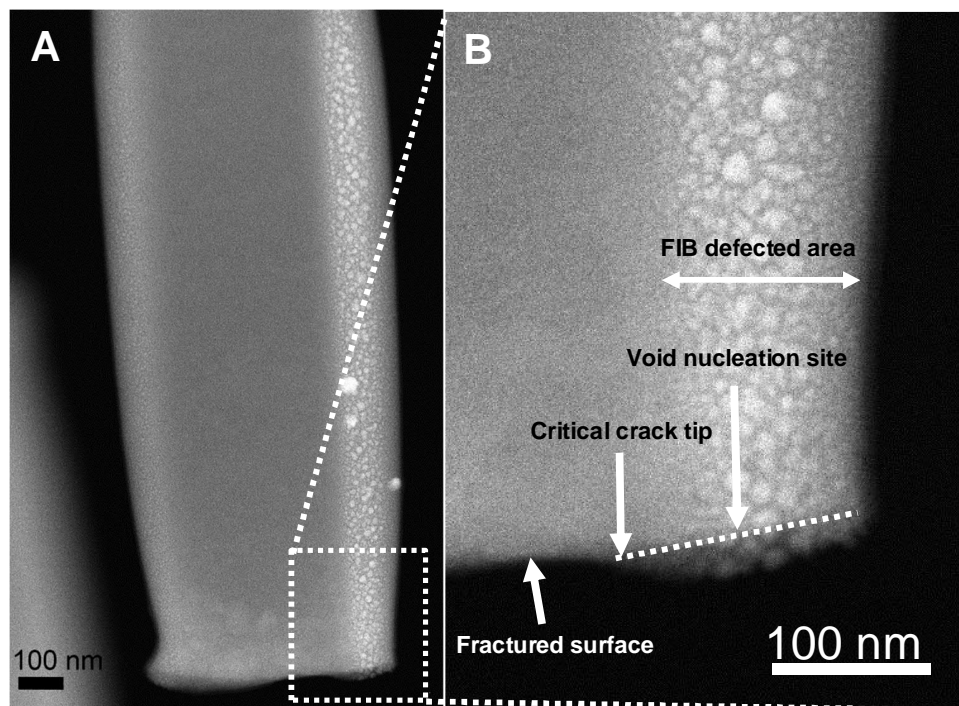
Fig. S8.

Origin of the void nucleation during tensile plastic flow. (A) STEM image of the fractured in situ tensile sample and (B) closer view on the fractured surface indicating the location of the void nucleation and the length of the propagated crack prior to final fracture.
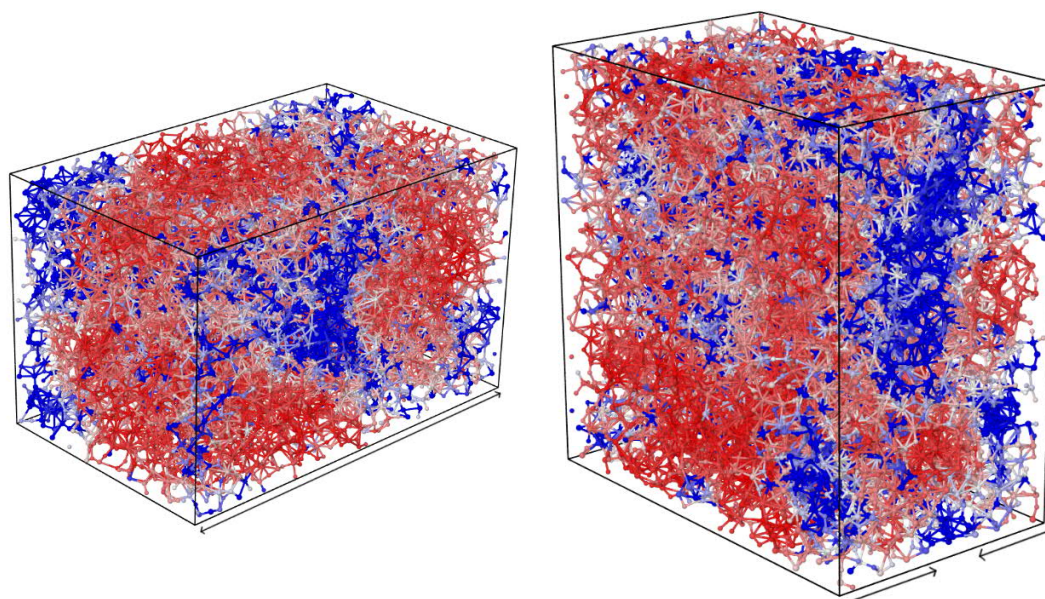
Fig. S9.

Distribution of local, momentary, plastic deformation in a-Al$_2$O$_3$. D$^2_{min}$ distribution in a-Al$_2$O$_3$ with $\Delta\varepsilon = 0.01$ in tensile loading at 0.3845 strain (left) and compressive loading at 0.3037 strain (right). Using a sliding color scale, atoms with below average D$^2_{min}$ are colored shades of red, average D$^2_{min}$ white, and above average D$^2_{min}$ shades of blue. Strain rate was 37.5 x 10^6 1/s. Loading axes shown by arrows.

5
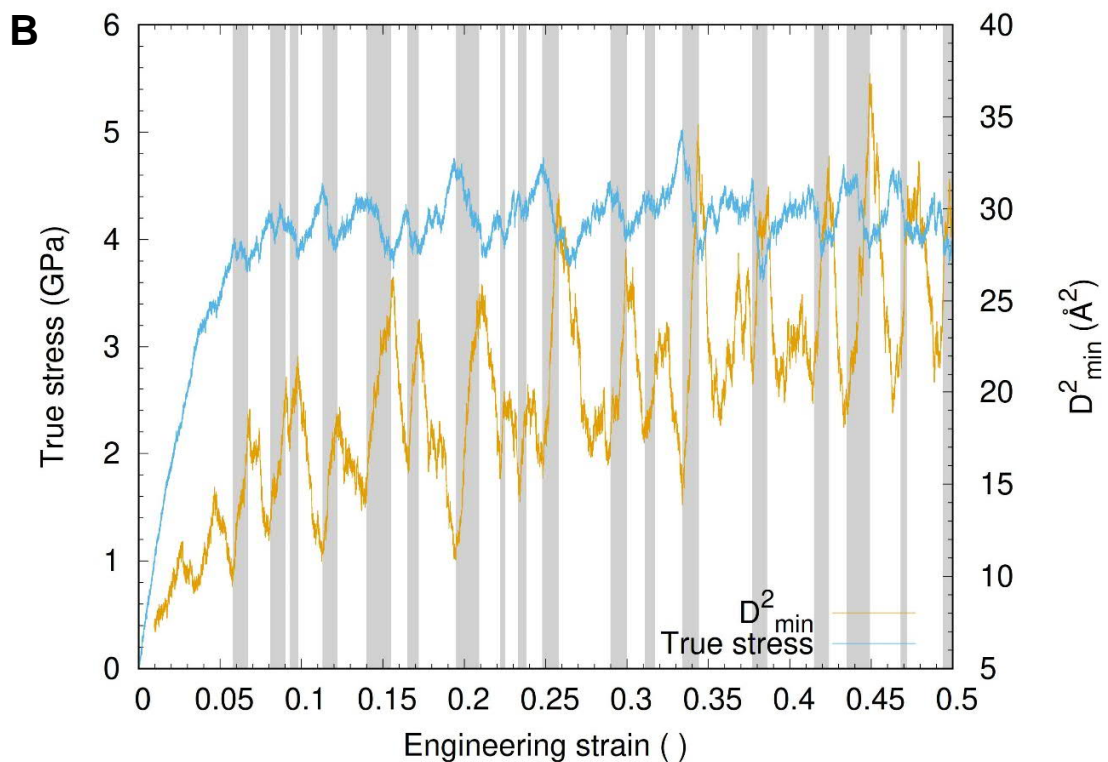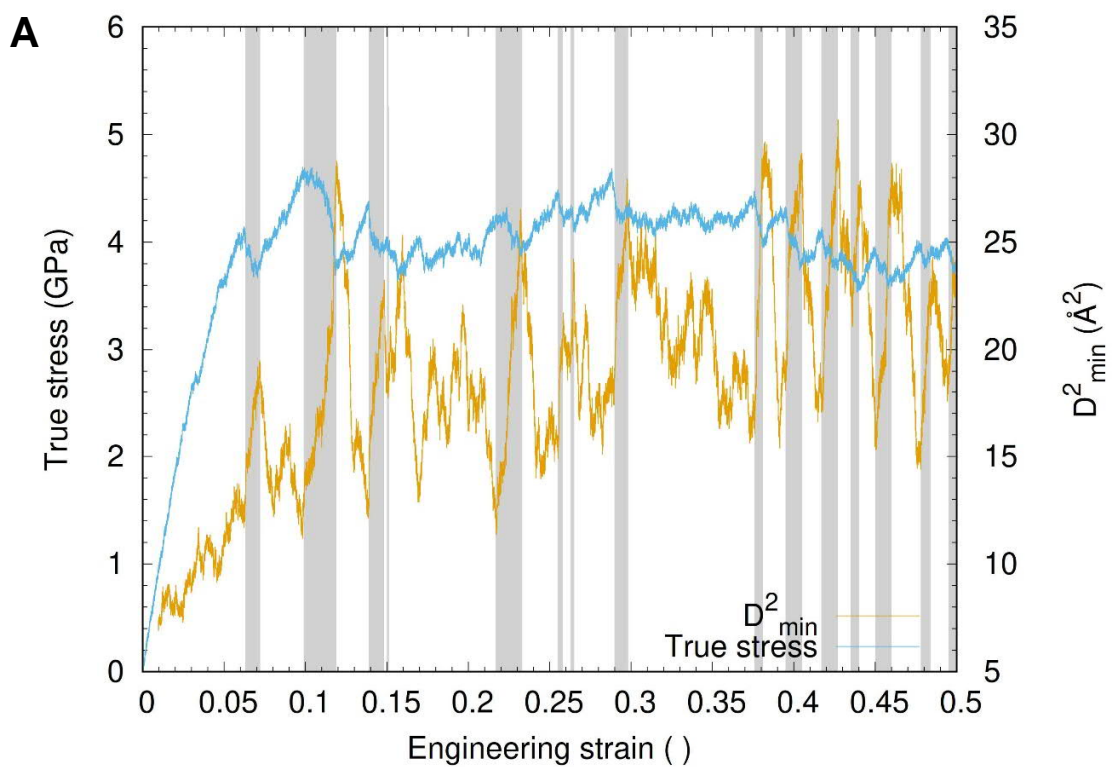
Fig. S10.

Correlation between local plastic strain events and stress as a function of strain in a-Al_2O_3. The momentary D^2_{min} ($\Delta\varepsilon = 0.01$) and true stress as a function of strain in (A) a single tension simulation and (B) a single compression simulation. Strain rate was 37.5 x 10^6 1/s. Momentary D^2_{min} data is set to start from 0.01 strain. Grey bands indicate strain section where the D^2_{min} is increasing in respect to stress.

5
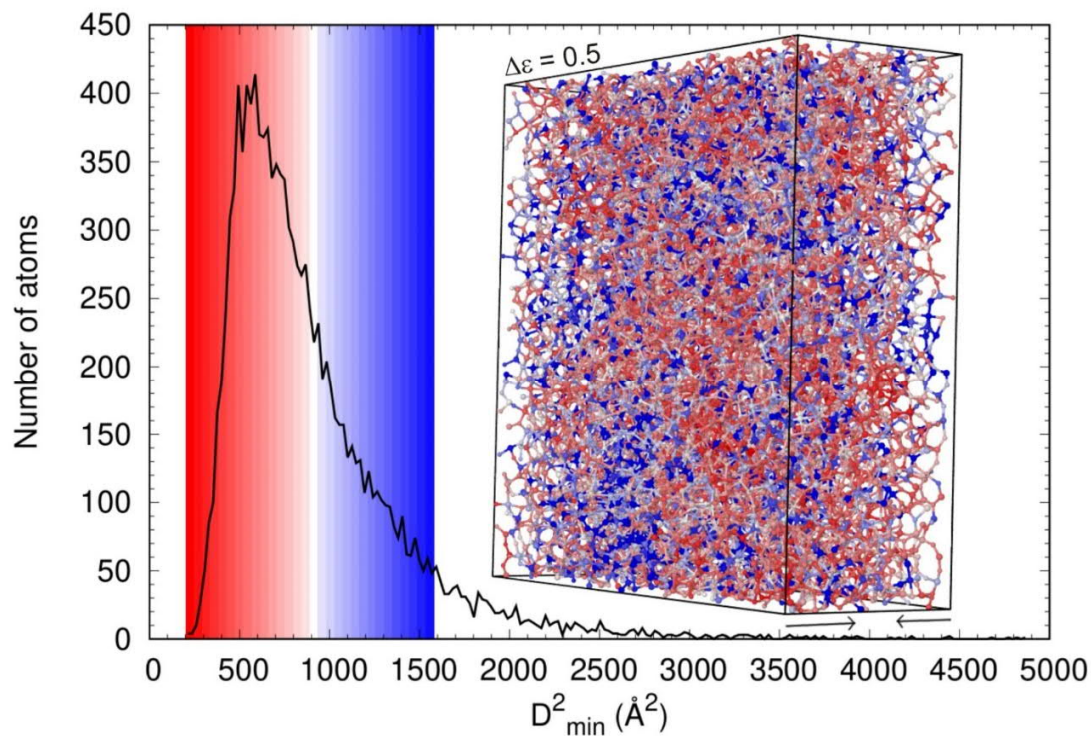
Fig. S11.

Cumulative distribution of local plastic strain in compression. Cumulative distribution of plastic compressive strain in the a-Al_2O_3 simulation cell between initial and final structure (D^2_{min}, $\Delta\varepsilon = 0.5$). Using a sliding color scale, atoms with below average D^2_{min} are colored shades of red, average D^2_{min} white, and above average D^2_{min} shades of blue. All atoms above the color scale are also colored blue. Strain rate strain rate was 7.5 x 10^7 1/s (N = 1). Loading axes shown by arrows.
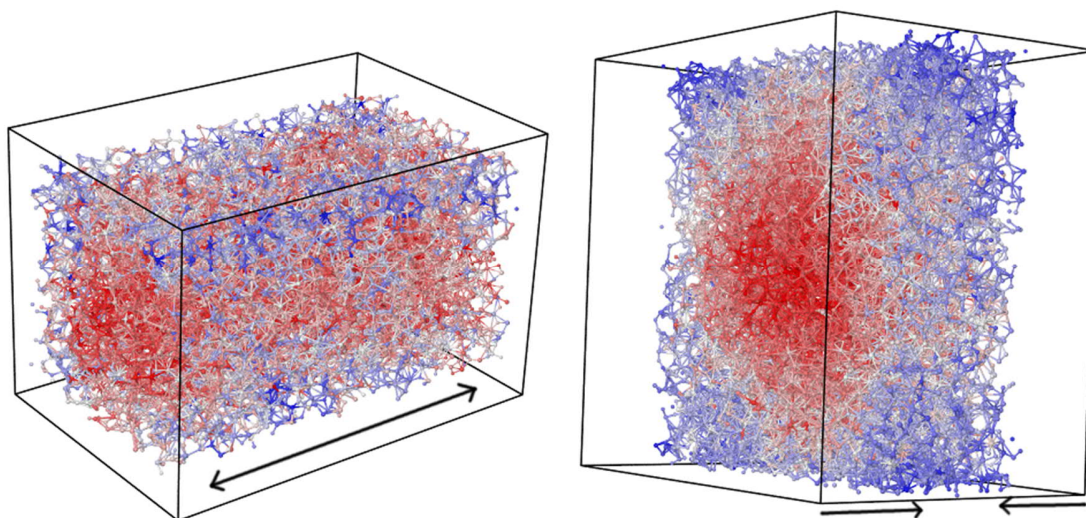
Fig. S12.

Mean-square displacement of atoms in a-Al_2O_3. The graph shows the MSD distribution of the
simulated atoms between initial and final structures ($\Delta\varepsilon = 0.5$). Using a sliding color scale,
atoms with low MSD are colored shades of red, medium MSD white and high MSD shades of
blue. Strain rate was 7.5×10^7 1/s. Loading axes shown by arrows.
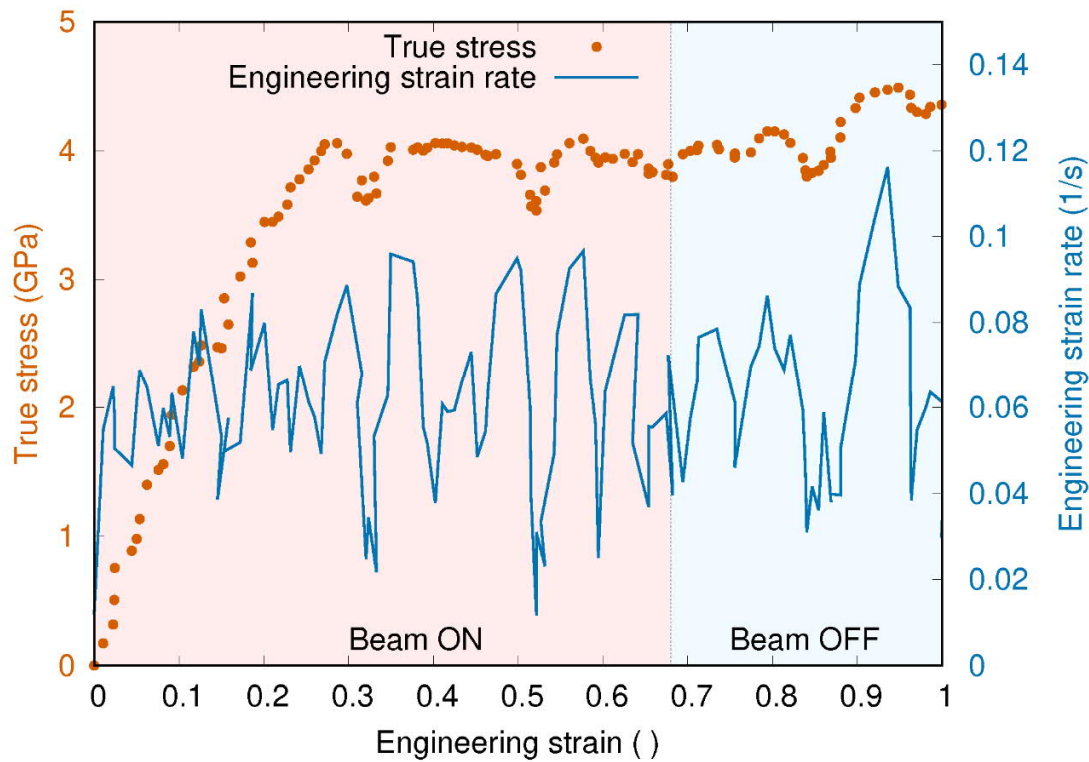
Fig. S13.

Effect of the electron beam on the mechanical response of a-Al$_2$O$_3$. Results on shear/compression experimental test (N = 1), where the TEM electron beam is ON from the beginning of the test and switched OFF at 0.68 strain. Strain rate data is filtered using the Savitzky-Golay method with 10 points of window and 5th polynomial order with the Origin software. Strain rate varies dynamically during the experimental measurement. True stress (GPa) on the left scale and engineering strain rate (1/s) on the right scale.
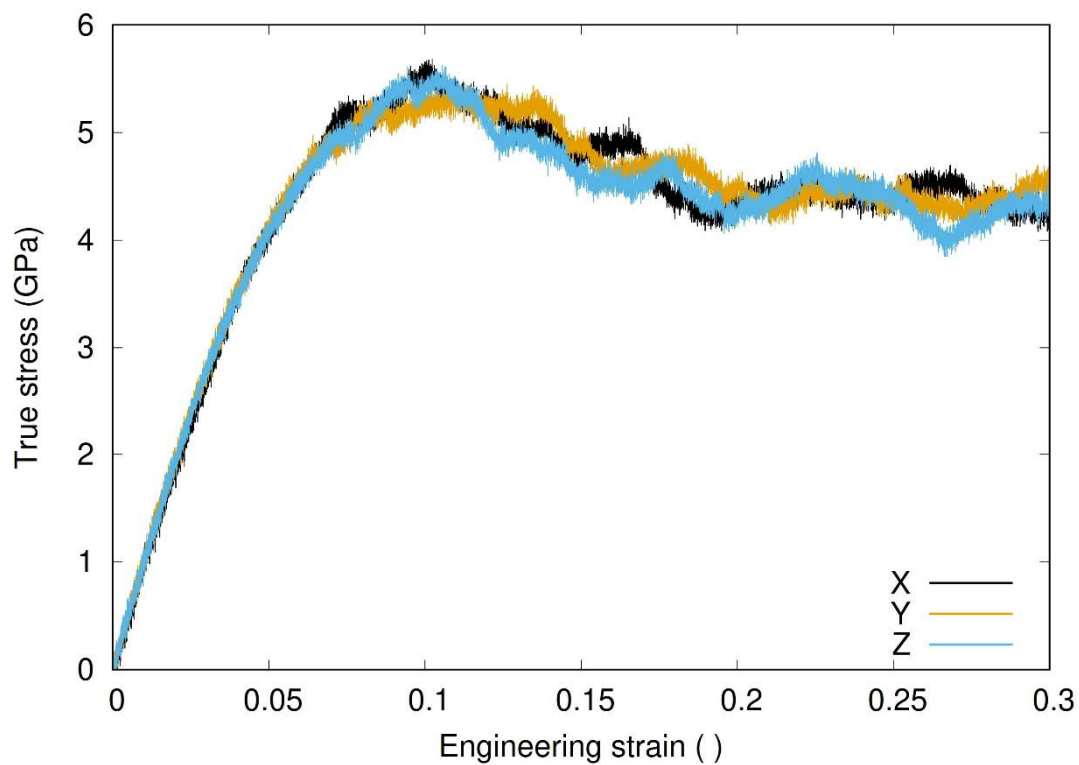
Fig. S14.

Stress-strain behavior of a-Al_2O_3 simulations with simulation parameters from Luo et al. (*24*). Labels X, Y and Z correspond to the longer dimension (110 Å) of the simulation cell (N =1).

5
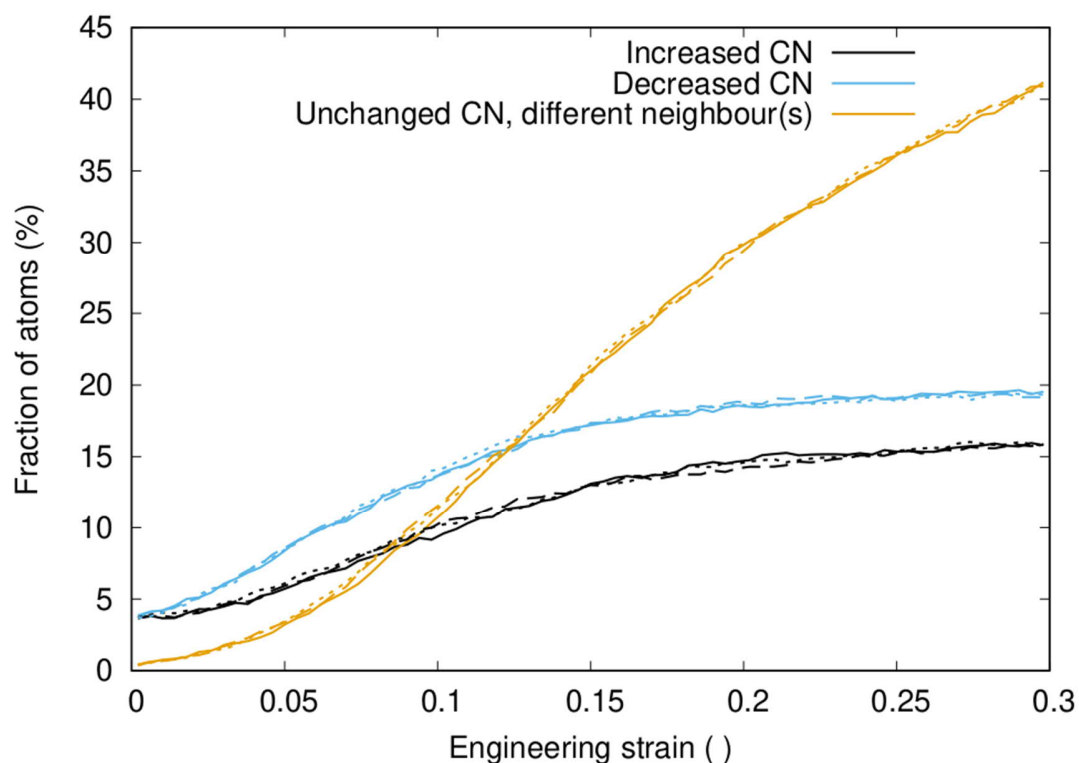
Fig. S15.

Bond switching in the three 110 x 55 x 55 Å tensile strain simulations. Increased/decreased CN means more/less atoms within 2.25 Å than in the initial structure of the simulation. Unchanged CN, different neighbors indicate the same number of atoms but at least one atom has been replaced by another. Solid lines is simulation where the long direction of the initial structure is along the X axis, long dashed line the simulation it is along the Y axis, and short dashed line the simulation where it is along the Z axis (N =1).
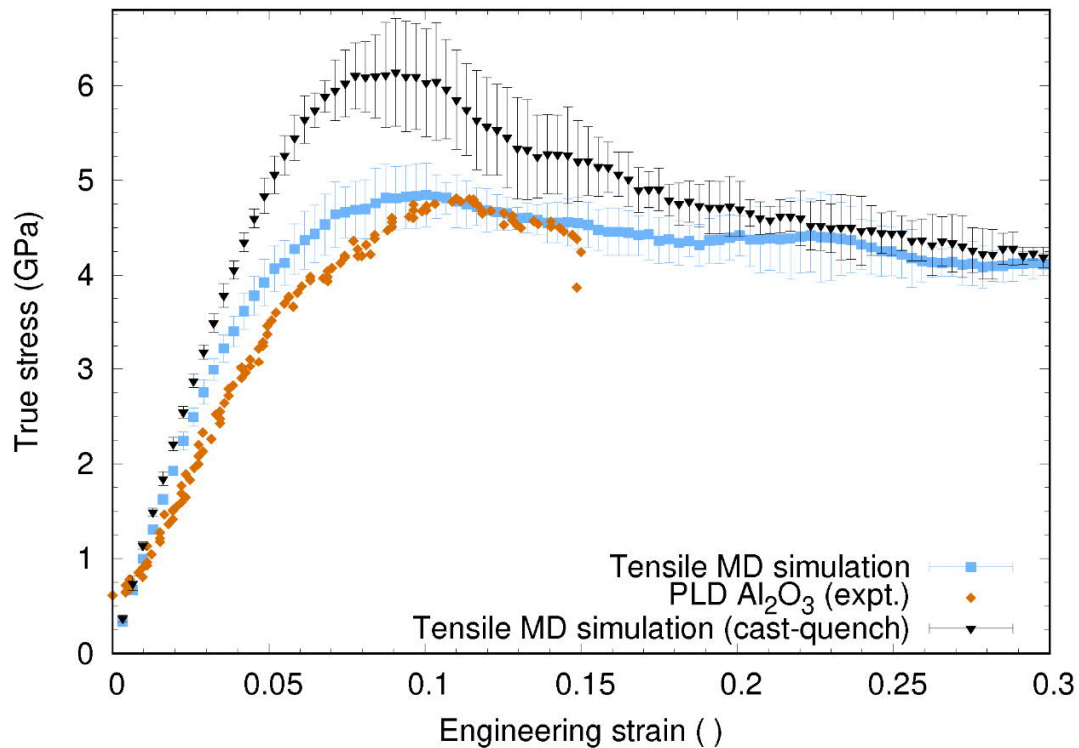
Fig. S16

Mechanical response comparison between originally quenched and cast-quenched structures to experimental data: Averaged simulated (original quench N = 24, cast-quench N = 12) and experimental (Beam ON, N = 1) tensile stress as a function of strain. Simulated error bars show the maximum variation measured with different strain rates (7.5 x 10^7 – 6.0 x 10^8 1/s).
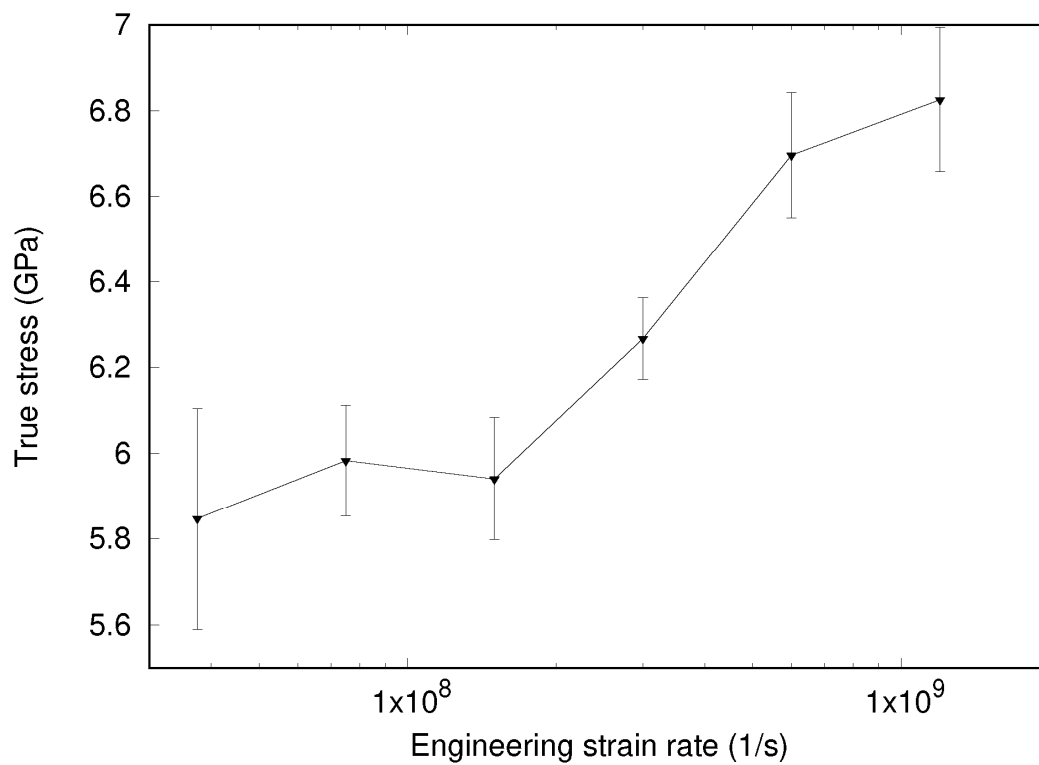
Fig. S17.

Yield stress (Peak stress, highest average stress over 0.01 strain sliding window) as a function of strain rate in tensile stress simulations with cast-quenched starting structure and different strain rates within range $37.5 \times 10^6 - 1.2 \times 10^9$ 1/s. Each data point is calculated from three simulations (N = 3).
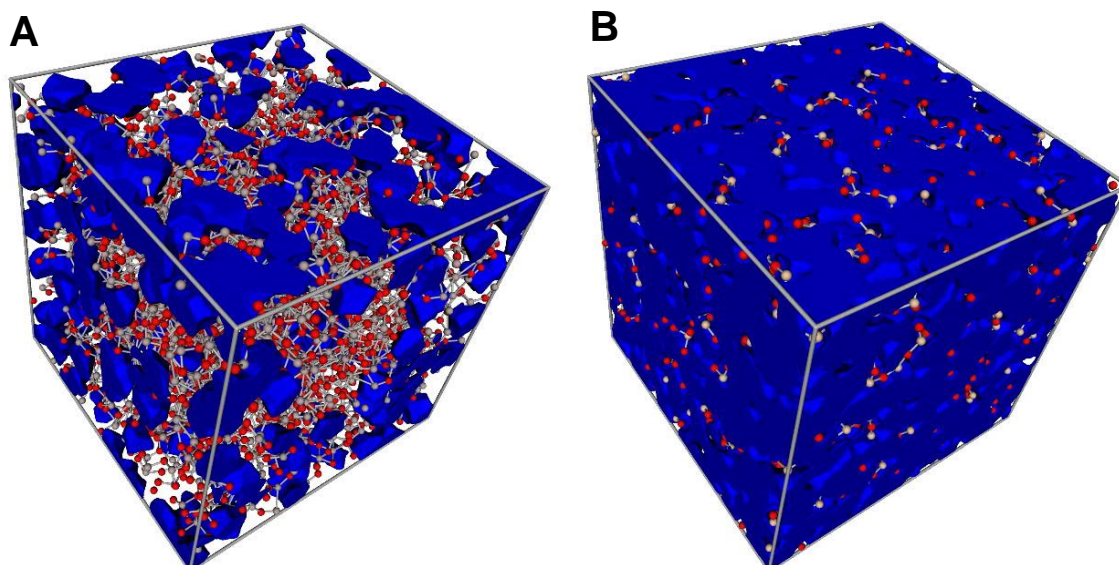
Fig. S18.

Pre-existing structural cavities in amorphous Al_2O_3 and amorphous SiO_2. (A) a-Al_2O_3 with 8.7 Vol. % of cavities (in blue). (B) a-SiO_2 with 65.7 Vol. % of cavities (30). Cut-off radii of test particles used for calculating the cavity volumes of a-Al_2O_3 (2.3 Å) and a-SiO_2 (2.1 Å) correspond to the first minimum of g(r) in both materials. Ambient pressure and temperature were used in both structures.
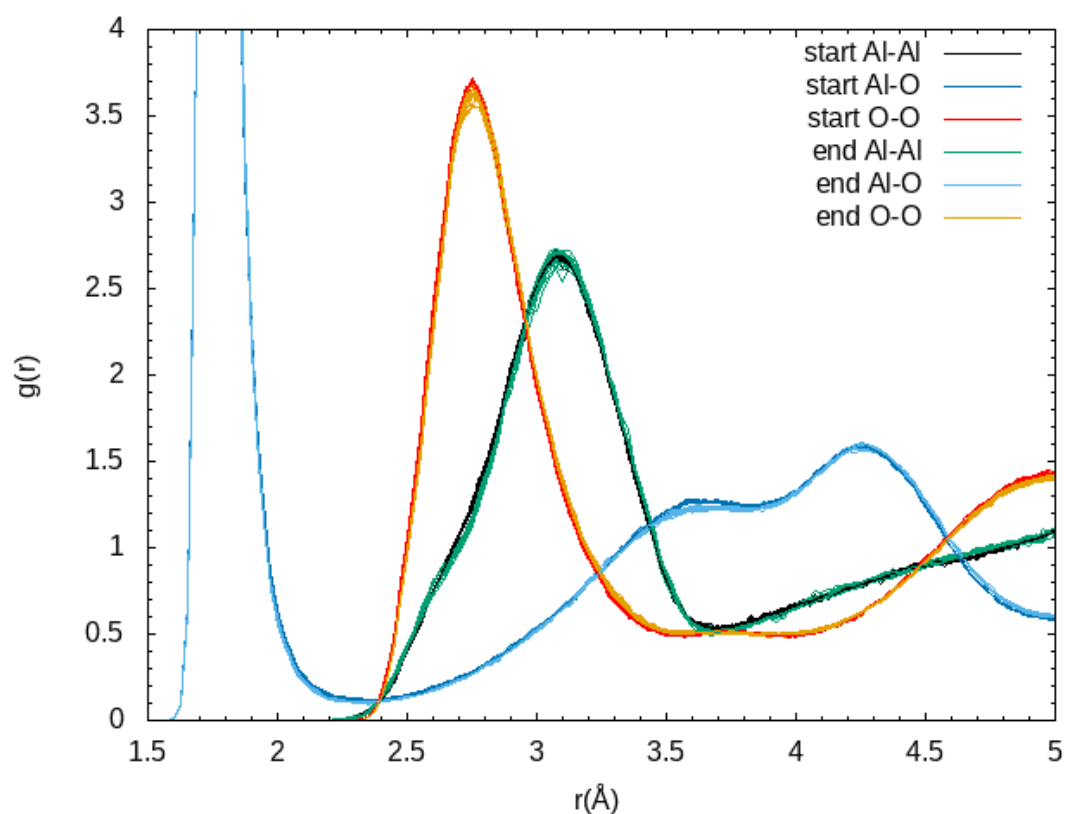
Fig. S19.

g(r) of the tensile strain simulations. The "start" graphs are average g(r) from the first 6 % (0.00 - 0.06) strain, and the end graphs are the average g(r) from the last 6 % (0.44 - 0.50) strain of each individual simulation (N =1).
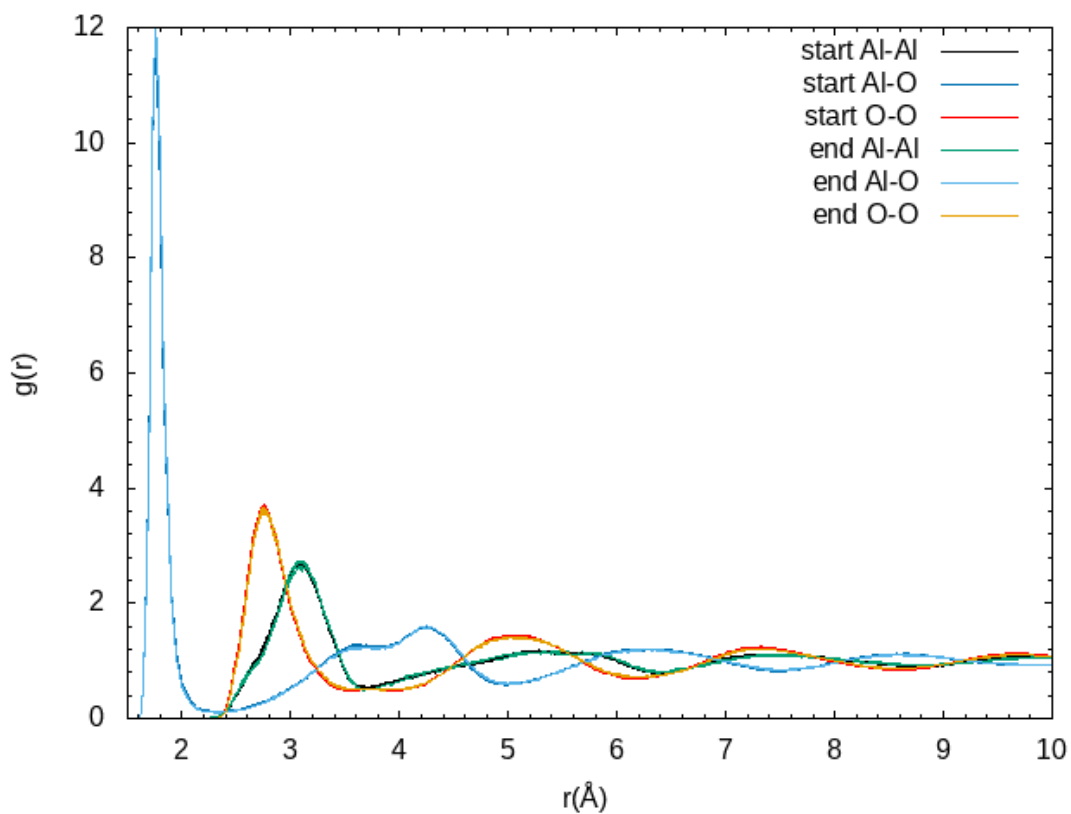
Fig. S20.

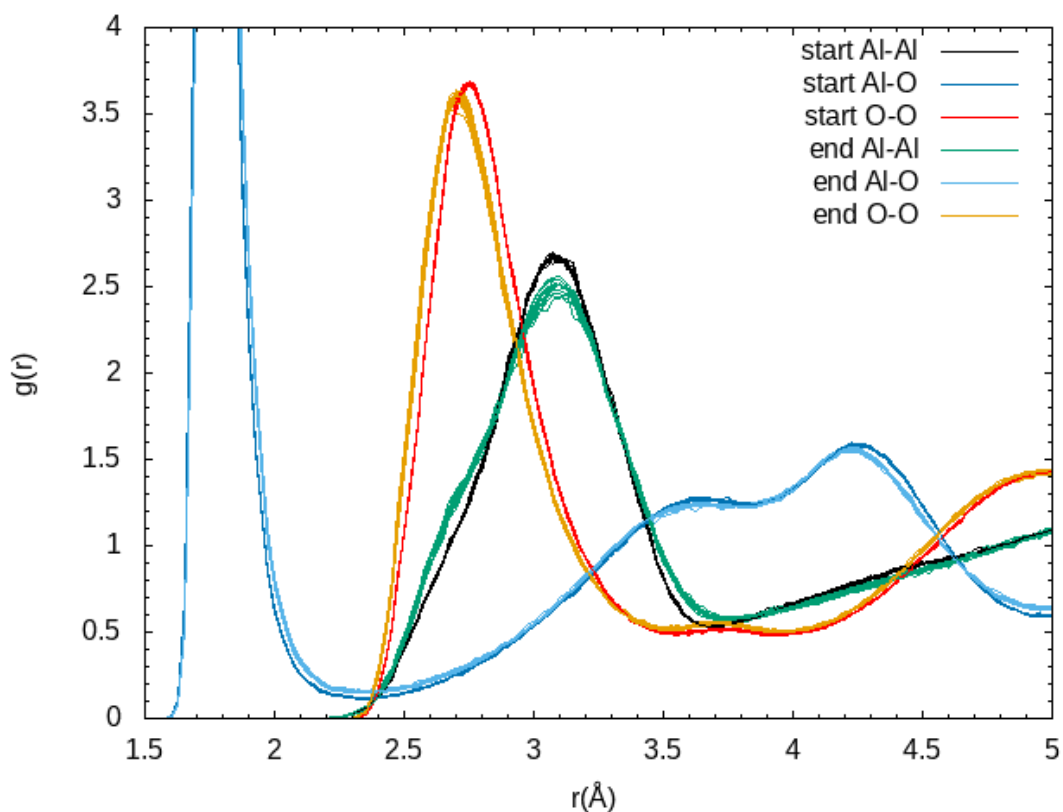Tensile simulation g(r) graph zoomed out on Fig. S16 to show the full first Al-O peak (N =1).

5

Fig. S21.

g(r) of the compressive strain simulations. The "start" graphs are average g(r) from the first 6 % (0.00 - 0.06) strain, and the end graphs are the average g(r) from the last 6 % (0.44 - 0.50) strain of each individual simulation (N =1).
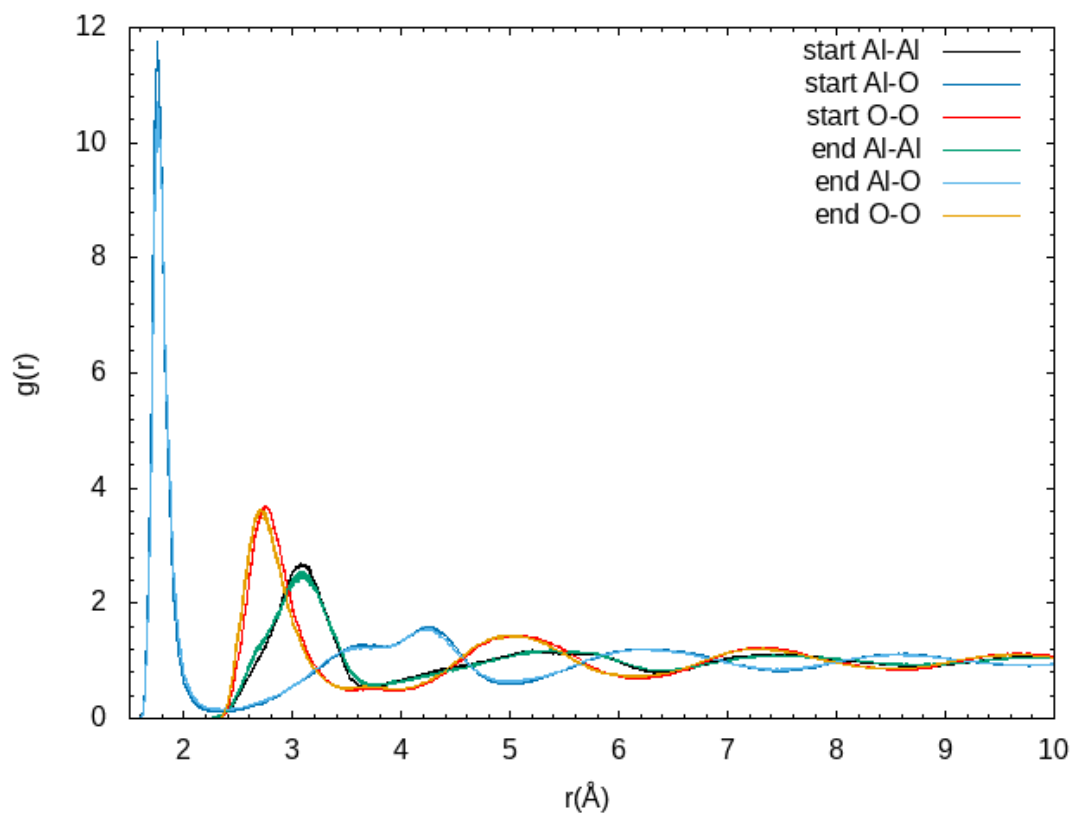
Fig. S22.

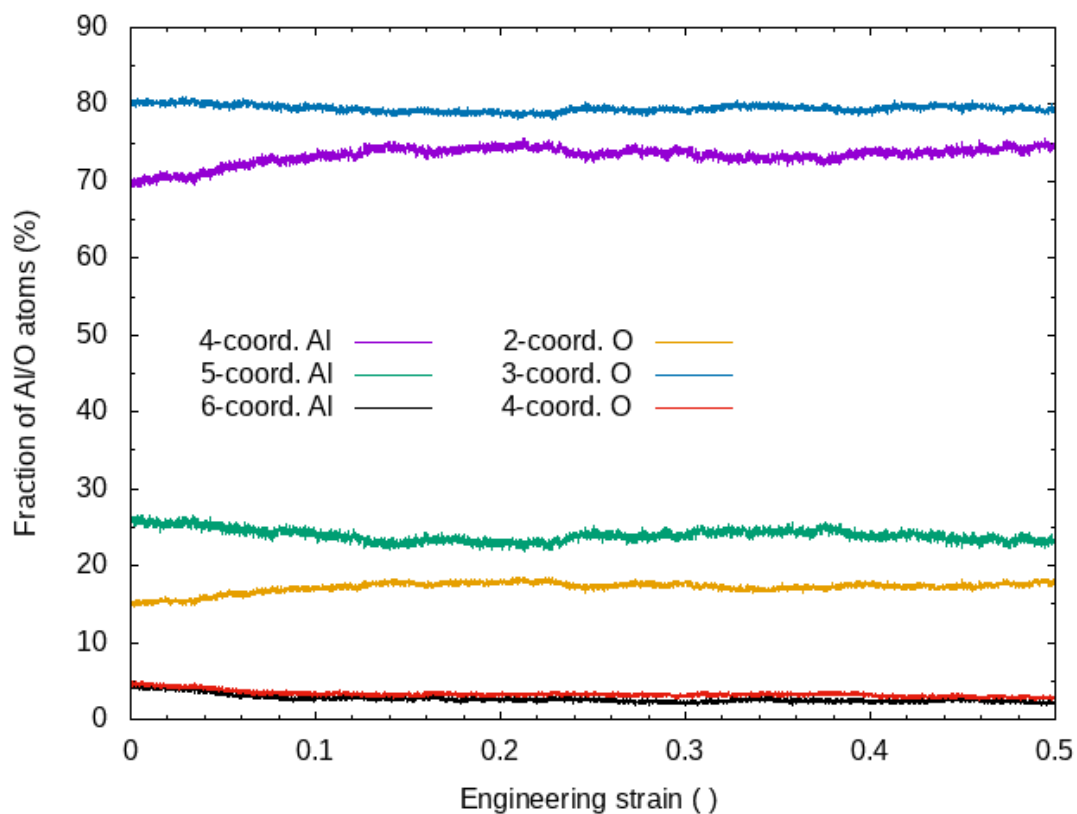Compression simulation g(r) zoomed out on Fig. S18 to show the full 1st Al-O peak (N =1).

Fig. S23.

An example of the evolution of the coordination distribution in tension. Taken from a 7.5×10^7 1/s simulation (N =1).
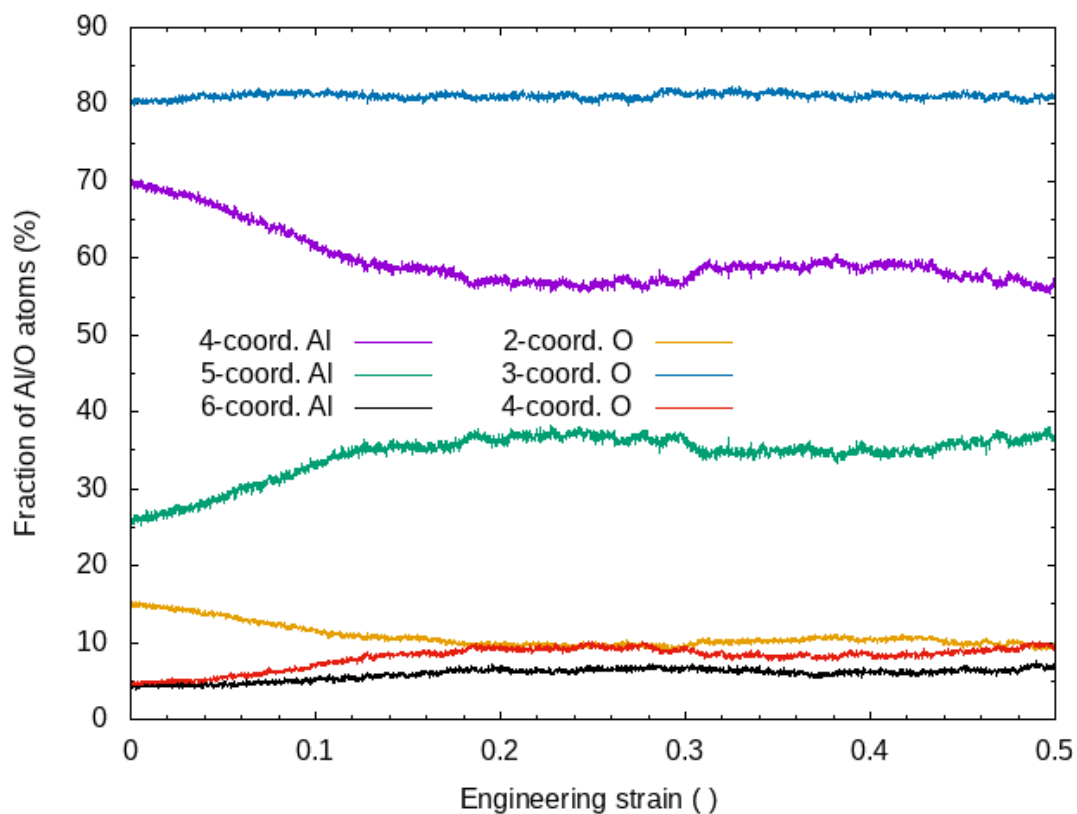
5

Fig. S24.

An example of the evolution of the coordination distribution in compression. Taken from a 1.5 x 10^8 1/s simulation (N =1).

5

Table S1.

Elastic moduli and Poisson's ratios for the used materials in FEM simulations.

	Elastic modulus (GPa)	Poisson's ratio ( )
Diamond	1200	0.22
Sapphire	350	0.30
Amorphous Al_2O_3 (16)	195.3 [70*]	0.294

* To study the effect of lower elastic modulus, 70 GPa was also used.

5

10

15

Table S2.

Plastic material model for FEM simulations of amorphous Al_2O_3.

Sy1 (Yield starts)	3 GPa
ep1 (Plastic yield at Sy1)	0
Sy2 (Flow stress)	4.5 GPa
ep2 (Plastic yield when Sy2 is reached)	0.847

5

Table S3.

Maximum theoretical temperature increase caused by the electron beam irradiation in amorphous Al_2O_3 during the in situ TEM experiments.

	Nakamura et al.(26)	Shear/compression	Tension	Remarks
R [m]	$6.4 * 10^{-5}$	$2.0 * 10^{-2}$	$1.35 * 10^{-6}$	Distance to the heat sink
r_0 [m]	$200 * 10^{-9}$	$500 * 10^{-9}$	$2.0 * 10^{-6}$	Measured from the TEM images
l_0 [m]	$15 * 10^{-9}$	$500 * 10^{-9}$	$42 * 10^{-9}$	Anvil tool under the film is thick
k [Wm^{-1}K^{-1}]	1.6	1.6	1.6	Sapphire tool has even higher k
φ [ ]	0.01	0.01	0.01	Fraction of the absorbed energy
V [V]	$2 * 10^6$	$3 * 10^6$	$3 * 10^6$	300 kV beam
ρ_0 [Am^{-2}]	600	4546	1	$I/\pi r_0^2$
I [A]	$7.5 * 10^{-11}$	$3.6 * 10^{-9}$	$4.6 * 10^{-12}$	Electron beam current on the specimen area
W_0 [W]	$1.50 * 10^{-7}$	$2.23 * 10^{-6}$	$5.36 * 10^{-6}$	Shear exp. sample exposed in a 75/360 ° sector. Tensile exp. sample covers roughly half of the irradiated area
T_{max} [K]	6	5	0.05	

5

Movie S1.

During tensile loading up to 0.5 strain, the localized plastic strain events vary randomly across the structure. Using a sliding color scale, atoms with below average D^2_{min} are colored shades of red, average D^2_{min} white, and above average D^2_{min} shades of blue. All atoms above the color scale are also colored blue.

5